

Dynamical masses and ages of Sirius-like systems

Hengyue Zhang (张恒悦)^{1,2★}, Timothy D. Brandt,¹ Rocio Kiman,³ Alexander Venner^{1,4}, Qier An,¹ Minghan Chen¹ and Yiting Li¹

¹Department of Physics, University of California, Santa Barbara, Santa Barbara, CA 93106, USA

²Sub-department of Astrophysics, Department of Physics, University of Oxford, Keble Road, Oxford OX1 3RH, UK

³Kavli Institute for Theoretical Physics, University of California, Santa Barbara, CA 93106, USA

⁴Centre for Astrophysics, University of Southern Queensland, Toowoomba, QLD 4350, Australia

Accepted 2023 June 15. Received 2023 June 15; in original form 2023 March 14

ABSTRACT

We measure precise orbits and dynamical masses and derive age constraints for six confirmed and one candidate Sirius-like systems, including the Hyades member HD 27483. Our orbital analysis incorporates radial velocities, relative astrometry, and *Hipparcos*–*Gaia* astrometric accelerations. We constrain the main-sequence lifetime of a white dwarf’s progenitor from the remnant’s dynamical mass and semi-empirical initial–final mass relations and infer the cooling age from mass and effective temperature. We present new relative astrometry of HD 27483 B from Keck/NIRC2 observations and archival *Hubble Space Telescope* data, and obtain the first dynamical mass of $0.798_{-0.041}^{+0.10} M_{\odot}$, and an age of 450_{-180}^{+570} Myr, consistent with previous age estimates of Hyades. We also measure precise dynamical masses for HD 114174 B ($0.591 \pm 0.011 M_{\odot}$) and HD 169889 B ($0.526_{-0.037}^{+0.039} M_{\odot}$), but their age precisions are limited by their uncertain temperatures. For HD 27786 B, the unusually small mass of $0.443 \pm 0.012 M_{\odot}$ suggests a history of rapid mass-loss, possibly due to binary interaction in its progenitor’s asymptotic giant branch phase. The orbits of HD 118475 and HD 136138 from our radial velocity fitting are overall in good agreement with *Gaia* DR3 astrometric two-body solutions, despite moderate differences in the eccentricity and period of HD 136138. The mass of $0.580_{-0.039}^{+0.052} M_{\odot}$ for HD 118475 B and a speckle imaging non-detection confirms that the companion is a white dwarf. Our analysis shows examples of a rich number of precise WD dynamical mass measurements enabled by *Gaia* DR3 and later releases, which will improve empirical calibrations of the white dwarf initial–final mass relation.

Key words: astrometry – binaries: general – stars: fundamental parameters – stars: imaging – stars: kinematics and dynamics – white dwarfs.

1 INTRODUCTION

While isolated white dwarfs (WDs) simply cool and fade indefinitely, WDs in binary systems can give rise to some of the most dramatic events in the Universe. These include novae and Type Ia supernovae, the source of much of the Universe’s iron-peak elements (Iwamoto et al. 1999) and standardizable candles used to measure the expansion history of the Universe (e.g. Phillips 1993; Riess et al. 1998; Perlmutter et al. 1999). The nearest known WD, Sirius B, is itself one component in a binary system (Bond 1862); it orbits 20 au (Bond et al. 2017) from the early A-type star (Morgan, Harris & Johnson 1953) Sirius A. Widely separated Sirius-like systems enable mass measurements based only on Newtonian dynamics and they form the widely separated analogues of the progenitors of novae and supernovae.

Stars below $\approx 8 M_{\odot}$ will end their lives as WDs, while stars below $\approx 0.8 M_{\odot}$ live longer than a Hubble time on the main sequence (MS), according to stellar evolutionary models (e.g. Choi et al. 2016). At least half of the stars in this mass interval are born in binaries (Raghavan et al. 2010). The Solar neighbourhood is rich in the Sirius-

like systems left after the more massive star in the binary has evolved off the MS. Before turning into a WD, the star loses mass by expelling its outer shell and exposing its central core during the asymptotic giant phase (see e.g. Höfner & Olofsson 2018 for a review). The final mass of the remnant WD is related to the initial mass of its progenitor by the initial–final mass relation (IFMR). Constraining the relation is crucial to understanding the complex physical processes underlying the final stages of stellar evolution. Observations of orbits of Sirius-like systems enable precise measurements of WD masses without requiring constraints on surface gravity and are independent of WD evolutionary models. Combining the mass with a T_{eff} or luminosity measurement constrains the WD’s cooling age, which informs us about the WD’s initial mass when compared to the age of the MS companion. These provide direct measurements of the IFMR. Conversely, one can derive the total age of the WD by assuming a particular IFMR. Comparing the WD’s age to the MS star’s age tests the accuracy of the assumed IFMR.

Fitting dynamical masses and orbits to Sirius-like systems requires either long-term astrometric monitoring like that available for Sirius (e.g. Bond et al. 2017), or the combination of different data types to compensate for limited phase coverage. On the one hand, absolute astrometry from the *Hipparcos* (ESA 1997) and *Gaia* (Gaia Collaboration 2016) missions probes the transverse

* E-mail: hengyue.zhang@physics.ox.ac.uk

acceleration of the MS star due to the tug of a WD companion. These powerful astrometric measurements have been compiled and calibrated to the same reference frame by the *Hipparcos-Gaia* Catalog of Accelerations (HGCA; Brandt 2018, 2021). On the other hand, spectrographs like the University College London Echelle Spectrograph (UCLES) on the Anglo-Australian Telescope (AAT; Diego et al. 1990), the High-Resolution Echelle Spectrometer (HIRES) at the Keck observatory (Vogt et al. 1994), the Levy spectrometer for the Automated Planet Finder (APF; Vogt et al. 2014), and the Hamilton Echelle Spectrometer at the Lick Observatory (Fischer, Marcy & Spronck 2014) provide high-precision radial velocities (RVs) that probe the MS star’s acceleration along the line of sight. These measurements, together with relative astrometry of a short orbital arc, enable a direct measurement of WD mass (e.g. Brandt, Dupuy & Bowler 2019; Bowler et al. 2021; Zeng et al. 2022).

In this paper, we combine absolute astrometry from the HGCA with RVs and relative astrometry from various sources to measure orbits and masses of six confirmed and one candidate nearby Sirius-like systems, including the Hyades member HD 27483. Here, we define a ‘Sirius-like system’ as any binary or multiple star system containing at least one WD and at least one non-compact star with spectral type earlier than M0, consistent with the definition in Holberg et al. (2013). For HD 118475 and HD 136138, we compare our results against *Gaia* DR3 two-body solutions (Gaia Collaboration 2023; Holl et al. 2023). We use the open source code ORVARA (Brandt et al. 2021b) to perform the fits and to derive constraints on the WDs’ masses and orbits. Then, we infer age constraints on four WDs from their dynamical masses and effective temperatures (T_{eff}).

We structure the paper as follows. Section 2 introduces our target selection method and summarizes the properties of the selected targets. In Section 3, we outline the observational data available for each target and present our new observation for HD 27483 and the corresponding data reduction. We introduce our orbit-fitting method and discuss our results in Section 4. In Section 5, we perform a Bayesian age analysis on the WDs and compare our results with existing age estimates by other methods. In Section 6, we discuss whether the progenitors of the WDs could have interacted with their companions. Then, we compute the radii of the WDs from photometry and spectroscopy and compare them to theoretical WD mass–radius relations (MRRs). We conclude in Section 7.

2 TARGET SELECTION

We selected our sample from the list of known Sirius-like systems in Holberg et al. (2013) and the more recently detected WD + early non-compact star binaries in the Montreal White Dwarf Database¹ (Dufour et al. 2017). Of more than 100 such systems, we first selected 62 targets that have astrometric accelerations in the HGCA (Brandt 2018, 2021). Then, we excluded 49 targets with neither high-precision RVs nor at least two epochs of relative astrometry. We choose not to redo the dynamical mass analysis for six systems that already have precise dynamical mass measurements: 40 Eri (Mason, Hartkopf & Miles 2017), Procyon (Bond et al. 2015), Sirius (Bond et al. 2017), Gl 86 (Brandt et al. 2019), and 12 Psc and HD 159062 (Bowler et al. 2021). In addition to the selection criteria, we removed HD 149499 as we found that its $\sim 0.45 M_{\odot}$ inner companion (Tokovinin et al. 2019) alone explains the host star’s astrometric acceleration and RV trend, which leaves almost no information to

¹<https://www.montrealwhitedwarfdatabase.org/home.html>

Table 1. Summary of host star properties.

HD	SpT	ϖ (mas)	M (M_{\odot})	Ref.
19019	G0 V	31.979 ± 0.029	1.06 ± 0.06	1
27483	F6 V + F6 V	21.094 ± 0.032	2.77 ± 0.26	2
27786	F4 IV-V	23.79 ± 0.11	1.54 ± 0.08	3
114174	G3 IV	37.868 ± 0.024	0.97 ± 0.04	4
118475	F9 V	29.537 ± 0.017	1.16 ± 0.06	3
136138	G8 IIIa	9.011 ± 0.051	1.84 ± 0.40	5
169889	G7 V	28.279 ± 0.026	0.98 ± 0.05	3

Note. The spectral types are collected from Skiff (2014) and parallaxes from *Gaia* DR3 (Gaia Collaboration 2023). The references for stellar masses are: 1. Landstreet & Bagnulo (2020); 2. Konacki & Lane (2004); 3. Kervella et al. (2019); 4. Rosenthal et al. (2021); and 5. Stefanik et al. (2011).

constrain the outer WD companion (first discovered by Jordan et al. 1997). Furthermore, we added HD 118475 B, an unconfirmed WD detected by RV in Kane et al. (2019). We ended up with seven targets, three of which have both high-precision RVs and relative astrometry, two of which only have relative astrometry (HD 27483 and HD 27786), and two of which (HD 118475 and HD 136138) only have RVs. The host star properties are summarized in Table 1. We collected the spectral types from Skiff (2014) and parallaxes from *Gaia* DR3 (Gaia Collaboration 2023). We adopted the most recent isochronological mass for each host star except HD 27483 A, for which we used the total dynamical mass of the two F6 V components of the spectroscopic binary, measured by Konacki & Lane (2004).

3 OBSERVATIONS AND DATA

We collect high-precision RVs, relative astrometry, and the *Hipparcos-Gaia* absolute astrometry to determine each system’s orbital parameters and masses. Because a WD companion is fainter than an MS companion with the same mass, it needs to be further from the primary star to be detectable by direct imaging. However, such a companion is often too widely separated to impose significant radial or astrometric acceleration on the primary star. Hence, high-precision RVs and multiple epochs of relative astrometry are not simultaneously available for more than half of our systems. Below we summarize the data that we adopted for each system. We use J2000 as the astrometric reference frame throughout this work.

3.1 Absolute astrometry

Absolute astrometry shows the proper motion anomaly of stars and is thus powerful in constraining the orbits of massive, long-period companions. We use the absolute astrometry in the EDR3 version of the HGCA (Brandt 2021), which calibrates *Gaia* EDR3 and *Hipparcos* astrometry to reveal the proper motion difference between *Hipparcos*, *Gaia*, and the *Hipparcos-Gaia* mean motion. This gives the astrometric acceleration of the host star, which is directly proportional to the companion’s mass. Table 2 lists the difference between the *Gaia* proper motion ($\mu_{\alpha\ast,\delta}^{\text{Gaia}}$) and the *Hipparcos-Gaia* mean motion ($\mu_{\alpha\ast,\delta}^{\text{H-G}}$) for each target, with the corresponding significance levels of astrometric accelerations. Five of our targets have levels $\gg 5\sigma$, meaning that they have accelerated significantly due to the gravitational pull of the companions.

We also checked *Gaia* DR3 for astrometric non-single stars among our targets. We found two-body fits (Holl et al. 2023) for HD 118475 and HD 136138, which significantly corrected the proper motion

Table 2. Proper motion anomaly ($\mu_{\alpha^*,\delta}^{\text{Gaia}} - \mu_{\alpha^*,\delta}^{\text{H-G}}$) of the targets as given by the HGCA.

HD	$\Delta\mu_{\alpha^*}$ (mas yr ⁻¹)	$\Delta\mu_{\delta}$ (mas yr ⁻¹)	Sig. level
19019	0.045 ± 0.049	-0.017 ± 0.040	0.7σ
27483	0.79 ± 0.06	2.15 ± 0.04	52σ
27786	-0.91 ± 0.21	-19.42 ± 0.13	150σ
114174	0.54 ± 0.04	-3.55 ± 0.04	88σ
118475	28.99 ± 0.51	18.37 ± 0.57	64σ
136138	-0.89 ± 0.30	-0.97 ± 0.32	4.1σ
169889	0.51 ± 0.04	-1.77 ± 0.04	48σ

and parallax measurements from their one-body fits. This suggests that the orbital periods of the two systems are comparable to the duration of the *Gaia* mission. For such systems, the proper motion of the primary star changes considerably between each scan of *Gaia*, making the *Gaia* one-body proper motion measurement, obtained by fitting a single proper motion value to data from multiple scans, hard to interpret before the release of *Gaia* intermediate astrometric data (IAD). The two-body proper motion, on the other hand, refers to the barycentre motion of the binary and contains no information on the orbit between the two stars. Therefore, we decided not to use these proper motions, fitting the two systems only from their RVs and the corrected parallaxes. Section 4.2 compares our best-fitting orbital parameters to the *Gaia* DR3 two-body solution. Checking the consistency between the two types of solutions helps validate *Gaia* two-body astrometry. The companion of HD 19019 is detected in *Gaia* at a separation of 11.7 arcsec. We use the *Gaia* proper motions of the companion, calibrated to the same reference frame as the primary using the prescription in Cantat-Gaudin & Brandt (2021), to help constrain the orbit.

3.2 Radial velocity and relative astrometry

Our RVs and relative astrometry come from various literature sources, archival data, and, in the case of HD 27483, new data. In this section, we summarize the data available for each system.

3.2.1 HD 19019

The HD 19019 system contains a strongly magnetic WD, its spectroscopic signature detected by Landstreet & Bagnulo (2020) with the Intermediate-dispersion Spectrograph and Imaging System (ISIS) on the William Herschel telescope (Boksenberg 1985). It has 17 RV observations between 2002 and 2014 (Butler et al. 2017) by the HIRES instrument on Keck (Vogt et al. 1994). The system is in the Washington Double Star Catalog as WDS J03038+0608, first resolved by *Gaia* DR2 and reported by Knapp & Nanson (2019) as a common proper motion pair. The WD companion was also detected in *Gaia* DR3, which gives a total of two epochs of relative astrometry with precisions better than 0.1 mas. The extreme precision dominates over the precision of the rest of the data, causing the orbital fit routine (described in Section 4) to ignore the RV and absolute astrometry and struggle to converge. We inflated the uncertainties of *Gaia* relative astrometry by a factor of 5 to account for potential systematics and to avoid convergence issues.

3.2.2 HD 27483

Boehm-Vitense (1993) discovered a WD companion to the Hyades F6 V binary from the *International Ultraviolet Explorer* (IUE)

spectrum of the system. The companion was then resolved twice by *HST* in 1999 July (Barstow et al. 2001) and 2011 November (in WFC3 F218W, unpublished, *HST* proposal 12606, PI Martin Barstow). We derive relative astrometry and photometry from the unpublished data, using the host star’s point spread function (PSF) as a template to fit the companion’s position and magnitude. We apply a least-squares routine, assuming uniform σ_{data} on the intensity at each pixel and demanding a reduced χ^2 of unity. We fit for three parameters: an offset in each of two directions, and a contrast. We estimate the uncertainty of a parameter by fixing all other parameters at their best-fitting values and finding the $\Delta\chi^2 = 1$ interval of the free parameter. The results are listed in the first row of Table 3. The two existing epochs of relative astrometry gave only loose constraints on the orbital parameters when we applied our orbit fitting procedure in Section 4.

To obtain additional relative astrometry and photometry, we observed HD 27483 on 2021 November 25 UT with the second generation of the near-infrared camera (NIRC2) and the natural guide star adaptive optics system at the Keck II telescope (Wizinowich et al. 2000). In the K_s filter, we took 21 deep exposures with an integration time of 0.18 s per coadd, 150 coadds, and 1024×1024 pixels, obtaining high S/N images for the companion, but with the host star saturated. We then took 11 shallow (0.006 s integration time per coadd, 150 coadds, 128×120 pixels) exposures with unsaturated host star PSFs. We used the unsaturated PSFs in shallow exposures as templates to fit both the host star and the companion in deep exposures. For the host star, we masked saturated pixels, fitting the template only to the outer, unsaturated speckles. By comparing the results from different PSF templates, we confirm that the uncertainties of the fit were smaller than 0.1 pixels in both directions.

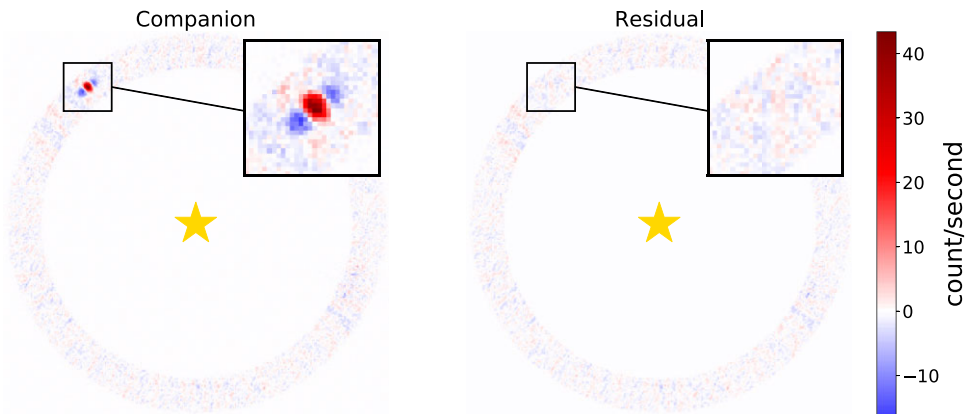
After centring the host star in each frame, we detected the companion by performing angular differential imaging (Marois et al. 2006, ADI) using the VIP-HCI (Gomez Gonzalez et al. 2017) package. Finally, we applied the negative fake companion method (Wertz et al. 2017, NEGFC) to fit the companion, subtracting the PSF template from the ADI annulus at different locations and magnitudes until minimizing the root-mean-square residual of the subtraction. We used the Markov chain Monte Carlo (MCMC) routine in VIP-HCI to perform the fit and estimate the uncertainties. We applied the distortion correction in Service et al. (2016), rotating the images by $\theta_{\text{north}} = 0.262^\circ \pm 0.020^\circ$ clockwise to align them with the celestial north. The plate scale we adopted is $9.971 \pm 0.004 \pm 0.001$ mas pixel⁻¹ (Service et al. 2016). We added these uncertainties to the uncertainties of the astrometry, in pixels, from the MCMC posteriors. The left-hand panel of Fig. 1 shows the ADI annulus, with the companion clearly revealed at a separation of 1.08 arcsec, and the right-hand panel shows the residual of the NEGFC subtraction. The derived relative astrometry and photometry are given in the second row of Table 3.

3.2.3 HD 27786

HD 27786 (56 Per) is a hierarchical four-body system with astrometric observations (e.g. Dembowski 1870; Rabe 1953; Kallarakal et al. 1969) dating back to 1847. Landsman, Simon & Bergeron (1996) first discovered an inner WD companion. Barstow et al. (2001) first resolved all four components, finding that the outer companion is itself two M dwarfs. From their astrometry and contrast values, we modelled the mass ratio between the two outer M dwarfs to be 1.475 ± 0.042 and derived that their barycentre is at a separation of

Table 3. New relative astrometry and photometry from this work.

Target	Date (UT)	Instrument	Sep (arcsec)	PA (deg)	Δm	Filter
HD 27 483	2011 Nov 26	WFC3	1.1880 ± 0.0038	25.32 ± 0.18	3.11 ± 0.17	F218W
HD 27 483	2021 Nov 25	NIRC2	1.0832 ± 0.0016	38.67 ± 0.07	7.79 ± 0.06	K_s
HD 27 786 Aa-Ab	2003 Jan 08	WFPC2	0.4120 ± 0.0070	288.56 ± 0.97	2.67 ± 0.22	F170W
Ba-Bb	2003 Jan 08	WFPC2	0.6200 ± 0.0096	290.18 ± 0.65	1.74 ± 0.22	F170W
Aa-B	2003 Jan 08	WFPC2	4.2924 ± 0.0072	14.31 ± 0.10	...	F170W
HD 27 786 Aa-Ab	2003 Dec 14	WFPC2	0.4024 ± 0.0096	280.41 ± 1.00	2.55 ± 0.24	F170W
Ba-Bb	2003 Dec 14	WFPC2	0.6173 ± 0.0059	289.23 ± 0.54	1.63 ± 0.23	F170W
Aa-B	2003 Dec 14	WFPC2	4.2681 ± 0.0071	14.11 ± 0.10	...	F170W
HD 27 786 Aa-Ab	2012 Feb 28	WFC3	0.2159 ± 0.0061	191.49 ± 1.62	4.64 ± 0.32	F218W
Ba-Bb	2012 Feb 28	WFC3	0.5272 ± 0.0041	273.22 ± 0.45	2.41 ± 0.17	F218W
Aa-B	2012 Feb 28	WFC3	4.2347 ± 0.0026	12.95 ± 0.04	...	F218W

**Figure 1.** PSF fitting for the NIRC2 observations of HD 27483. The left-hand panel shows the annulus obtained by performing ADI on the data cube. The companion (enlarged in the figure inset) is detected at a separation of 1.08 arcsec. The right-hand panel shows the residual of subtracting the best-fitting fake companion from the annulus. The host star, represented by a star symbol, is at the centre of the annulus.

4.325 arcsec and a PA of 14.95° relative to the host star. This allows us to treat the outer binary as a single companion and perform a three-body fit.

Unpublished observations by *HST* resolved the system twice in the WFPC2 F170W filter in 2003 January (*HST* proposal 9334, PI Howard Bond) and 2003 December (*HST* proposal 9964, PI Howard Bond) and once in the WFC3 F218W filter in 2012 February (*HST* proposal 12606, PI Martin Barstow). We derived relative astrometry and photometry from these unpublished observations using methods similar to that for the HD 27 483 *HST* observation. The only difference is that the WD companion is too close to the host star that we cannot use the host star PSF as a template. Instead, we adopted the observation of HIP 66 578 on 2000 January 18 (*HST* proposal 8496, PI Stefano Casertano) as the PSF template for WFPC F170W observations and the previously analysed image of HD 27 483 A as the PSF template for the WFC3 F218W observation. We find that adopting a different image as the PSF template results in positional differences of up to 7 mas, comparable to our statistical uncertainties. We add this to our error budget. The results are listed in Table 3.

Other epochs of relative astrometry did not resolve all four components and only measured the photocentre of the outer binary, which has a filter-dependent offset from the barycentre. We chose not to include them in the fit.

3.2.4 HD 114174

We have 66 high-precision RV measurements between 1997 and 2019, all of which are from HIRES as part of the California Legacy Survey (Rosenthal et al. 2021). Relative astrometry of the system consists of four observations by Crepp et al. (2013) in 2011 (first discovery) and 2012, one from Matthews et al. (2014) in 2013, one from Bacchus et al. (2017) in 2014, and 18 observations by Gratton et al. (2021) between 2014 and 2019 using the Spectro-Polarimetric High-contrast Exoplanet REsearch (SPHERE; Beuzit et al. 2019) instrument at the Very Large Telescope (VLT).

3.2.5 HD 118475

Kane et al. (2019) acquired RV data of the system using the UCLES high-resolution spectrograph (Diego et al. 1990) on the AAT. The data consist of 11 observations from 2002 to 2014 and reveal a companion with a minimum mass of $0.445 M_\odot$. Kane et al. (2019) found that a $0.445 M_\odot$ M dwarf would be inconsistent by 3.3σ with the non-detection in their 880 nm direct imaging observations, showing evidence that the companion is a compact object.

3.2.6 HD 136138

de Medeiros & Mayor (1999) first identified the system as a spectroscopic binary using RV observations, and the RV orbit was derived by Massarotti et al. (2008) and Griffin (2009). The *IUE* spectrum of the system shows that the companion is a hot ($T_{\text{eff}} = 30400 \pm 780$) WD (Stefanik et al. 2011). Stefanik et al. (2011) acquired 46 additional measurements of the RV between 2003 and 2009 using the Harvard–Smithsonian Center for Astrophysics Digital Speedometers (Mayor 1985; Latham 1992). We adopt all of them in our fit. Previous RVs dating back to 1924 are available in Griffin (2009), but we did not include those data because their measurement uncertainties are unavailable.

3.2.7 HD 169889

We have five epochs of relative astrometry published by Crepp et al. (2018), who first discovered the WD companion. Four observations were conducted using the NIRC2 instrument on Keck, and the observation on 2016 June 20 UT came from the Large Binocular Telescope mid-infrared camera (LMIRCam; Skrutskie et al. 2010). Eight precise RV measurements were obtained with HIRES in the California Planet Survey (Howard et al. 2010), showing a significant RV trend.

4 ORBIT FITTING

4.1 Method

We use the orbit-fitting code ORVARA (Brandt et al. 2021b) to infer the orbital parameters of each system. ORVARA implements a parallel-tempered MCMC with PTMCEE (Foreman-Mackey et al. 2013; Vousden, Farr & Mandel 2016, 2021). At each chain step, it uses HTOF (Brandt, Argafal & trace andreason 2021a) to model the positions and proper motions of the host star relative to the system’s barycentre as they would be seen by the *Hipparcos* and *Gaia* intermediate data. ORVARA then computes the likelihood of each sample orbit given the relative astrometry, HGCA absolute astrometry, and RVs.

We run the MCMC with 20 temperatures, 100 walkers per temperature, and at least 100 000 steps per walker. We discard at least the first 25 per cent and up to the first 75 per cent of the chain as the burn-in. Finally, we thin the chain by a factor of 50. We confirm that the chains have converged by reading ORVARA’s diagnostic plots that show the path of each walker in the parameter space, checking that every walker has reached the same posterior and has fully sampled the posterior.

We impose Gaussian mass priors on the host stars, adopting masses in Table 1, but use $1/M$ mass priors for the companions unless otherwise stated in Section 4.2. A dynamical mass prior is available for HD 27 483 A because the star is itself a spectroscopic binary with *Hipparcos* astrometry (Konacki & Lane 2004). For stars without previous dynamical mass measurements, we use their most recent isochronological masses as priors. We adopt the *Gaia* DR3 parallaxes as our parallax priors. We assume the standard geometric prior for the inclination and loguniform priors for the semimajor axis and the RV jitter. We use uniform priors for all other parameters.

4.2 Results

Our MCMC analysis improves the orbital parameters and gives unprecedented dynamical mass constraints for all systems except HD

118 475 and HD 136138, for which we have imprecise minimum masses due to not using *Hipparcos–Gaia* proper motions. Fig. 2 shows the best-fitting relative astrometric orbits of the systems. Fig. A1 is the corner plot of the key orbital parameters of HD 19019. Fig. A2 gives the best-fitting RV orbit of HD 19019 and the corresponding residuals. Fig. A3 shows the fit to relative and absolute astrometry of HD 19019 and the corresponding residual. Similar plots for other systems are available as supplementary material in the online version of the paper. Tables A1–A7 list the priors and posteriors of fitted and derived parameters of all seven systems. We discuss the details of each system below.

4.2.1 HD 19019

The dynamical mass constraint on the WD is loose because of the system’s long orbital period and insignificant astrometric acceleration. We place a uniform prior instead of a $1/M$ prior on the companion because the $1/M$ prior would dominate over the weak dynamical mass constraint and give a mass posterior very close to zero. The companion mass posterior of $0.32^{+0.37}_{-0.23} M_{\odot}$ is surprisingly in tension with (2σ away from) the spectroscopic mass of $1.12 \pm 0.15 M_{\odot}$ in Landstreet & Bagnulo (2020) and does not rule out $M_{\text{comp}} = 0$. The left-hand panel of Fig. A2 shows that the RV data cover only a tiny fraction of the orbit with an insignificant RV trend. Our best-fitting RV jitter of $12.2^{+2.6}_{-2.0} \text{ m s}^{-1}$ is within the error bars of the jitter of $13.36 \pm 2.86 \text{ m s}^{-1}$ derived by Luh et al. (2020) that assumed no companions, suggesting that the companion does not induce a measurable RV signal. The proper motion of the $G = 6.8$ star in *Gaia* DR4 will likely be ~ 4 times more precise than that in *Gaia* DR3 (Gaia Collaboration 2023). The uncertainties will be better than 0.01 mas yr^{-1} and comparable to the star’s proper motion change over the baseline of the *Gaia* mission, allowing substantial improvement in the system’s orbital parameters.

4.2.2 HD 27483

The host star, HD 27 483 A, is itself a tight binary of roughly equal masses and magnitudes, with a period of 3.06 d (Konacki & Lane 2004). We treat the host binary as a single star because the photocentre of its two components almost coincides with the barycentre.

The WD companion, HD 27 483 B, has a long history of spectroscopic observations. Boehm-Vitense (1993) derived a mass of $\sim 0.6 M_{\odot}$ from the WD’s *IUE* spectrum. Burleigh, Barstow & Holberg (1998) re-analysed the spectrum and got $M_{\text{WD}} \approx 0.94 M_{\odot}$. Joyce et al. (2018) analysed two *HST* spectra of the WD and got 0.748 ± 0.072 and $0.711 \pm 0.137 M_{\odot}$, respectively.

With a $1/M$ prior, our dynamical mass posterior of $0.798^{+0.10}_{-0.041} M_{\odot}$ agrees reasonably with and has comparable precision to the spectroscopic masses in Joyce et al. (2018). Compared to Burleigh et al. (1998), the smaller WD mass implies a longer progenitor lifetime and would bring the total age of the WD to closer agreement with that of the Hyades cluster. We perform a detailed analysis of the WD’s age in Section 5.3.2. The WD’s orbital inclination of $30^{\circ}_{-15^{\circ}}^{+13^{\circ}}$ is reasonably aligned with the inclination of the host binary’s orbit, $45.1^{\circ} \pm 1.7^{\circ}$ (Konacki & Lane 2004). Using a uniform companion mass prior instead of the log-flat prior does not change the MCMC posterior noticeably.

4.2.3 HD 27786

While HD 27 786 is a quadruple system, we treat the tight outer M dwarf binary as a single unit and perform a three-body fit with the

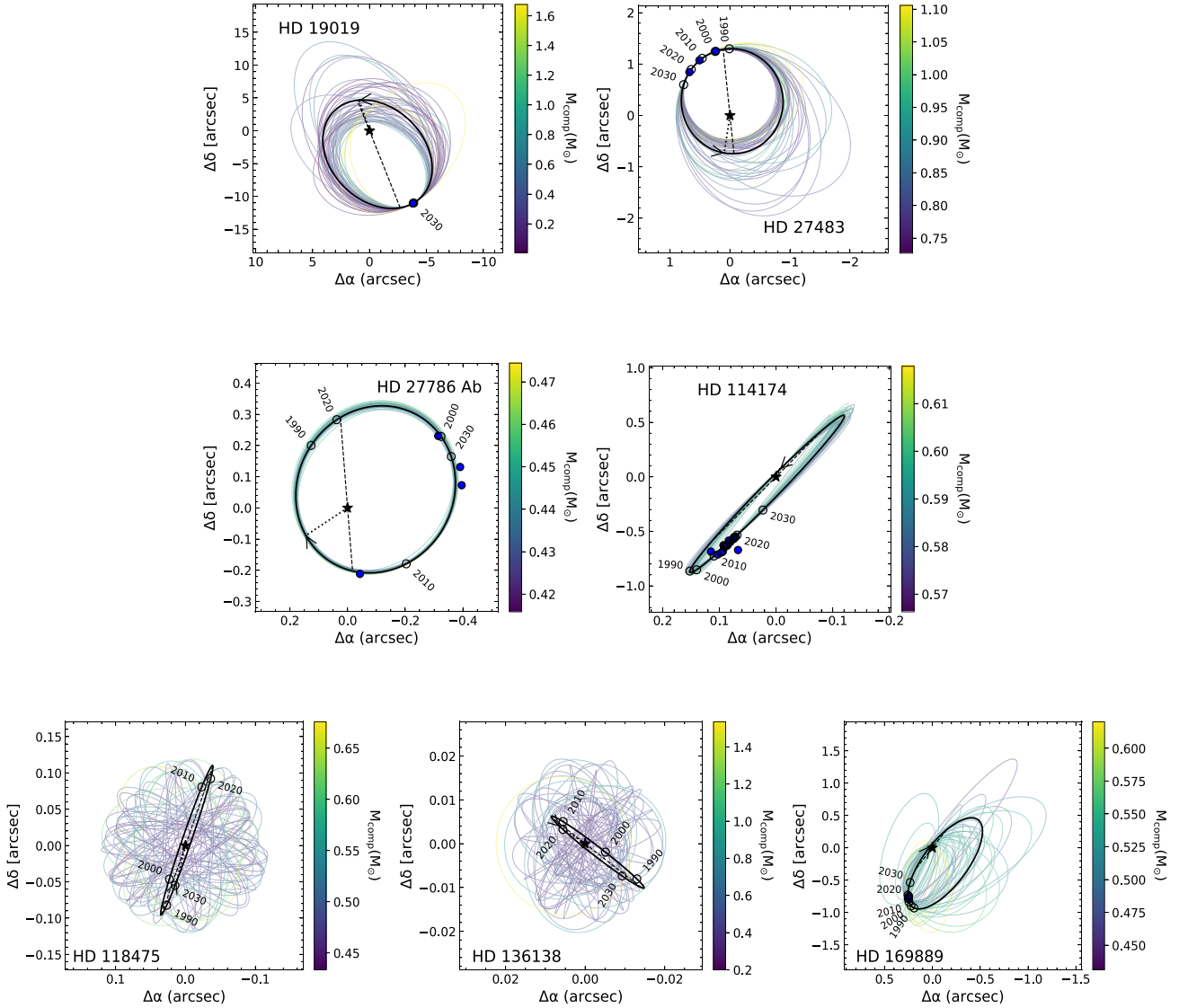


Figure 2. Relative astrometric orbits of companions. The thick black line indicates the maximum likelihood orbit. The thin lines, colour-coded by the companion mass, are 50 orbits drawn randomly from the posterior distribution. The dotted line connects the primary star to the periastron. The dashed line is the intersection between the orbital plane and the sky plane. The blue dots show the relative astrometry measurements, with error bars typically smaller than the size of the symbols. The black circles give the predicted positions of the companion at several past and future times along the orbit.

primary and the inner WD companion. We place a uniform mass prior on the outer binary. The three-body fit to the system has 16 separate parameters and is therefore difficult to converge. Hence, we adopt the orbital parameters for the outer companion in Tokovinin & Kiyaveva (2016) as the starting condition for the MCMC to speed up convergence.

Our dynamical mass of $M_{\text{WD}} = 0.443 \pm 0.012 M_{\odot}$ places the companion near the low-mass end in the known sample of WDs. Landsman et al. (1996) fitted possible spectroscopic masses of the WD for a grid of assumed distances. On their grid, the closest point to the *Gaia* DR3 distance of 42.0 ± 0.2 pc was at 43 pc, for which they derived a mass of $0.435 M_{\odot}$. The mass is within 1σ of our dynamical mass.

If we assume a standard evolutionary track, such a small dynamical mass implies a $<1 M_{\odot}$ progenitor, which does not have enough time to evolve off the MS within the primary star's age of $2.11^{+1.26}_{-0.79}$ Gyr (David & Hillenbrand 2015). One plausible explanation

is that the WD had a $\sim 2 M_{\odot}$ progenitor but underwent faster-than-usual mass-loss in its asymptotic giant branch (AGB) phase due to interactions with the primary star, such as common envelope evolution (see Ivanova et al. 2013, for a review). This scenario is not uncommon in compact binary systems with periods of days (Kilic et al. 2007; Brown et al. 2011) but is not known to happen for wider WD companions. Future spectroscopic observations of the system may provide evidence for or against such interaction.

Because the inner WD companion contributes > 99 per cent of the astrometric acceleration, it is unrealistic to tightly constrain the mass of the outer binary companion. The dynamical mass of $1.36^{+0.51}_{-0.41} M_{\odot}$ agrees loosely with the total photometric mass of the two companions, $0.84 M_{\odot}$ (Tokovinin & Kiyaveva 2016). Our result of $P = 1400 \pm 200$ yr and $a = 4.4 \pm 0.4$ arcsec is marginally consistent with $P = 1945 \pm 535$ yr and $a = 7.5 \pm 2.7$ arcsec from Izmailov (2019).

4.2.4 HD 114174

Literature spectroscopic masses of the WD companion are discrepant, depending on assumptions on core composition and the specific WD-evolution model applied. Matthews et al. (2014) reported a mass of $0.54 \pm 0.01 M_{\odot}$ using the theoretical models in Tremblay, Bergeron & Gianninas (2011) for a pure-H atmosphere and a C/O core. Bacchus et al. (2017), however, added new spectroscopy and got $M = 0.336 \pm 0.014 M_{\odot}$ for low-mass He-core evolutionary models (Althaus, Serenelli & Benvenuto 2001) and $M = 1.198 \pm 0.006 M_{\odot}$ for high-mass C/O core evolutionary models (Fontaine, Brassard & Bergeron 2001). Recent observations with SPHERE (Gratton et al. 2021) gave $M = 0.75 \pm 0.03 M_{\odot}$, derived from pure-H C/O core models in Bergeron, Wesemael & Beauchamp (1995). The only previous measurement of the companion’s dynamical mass was from Crepp et al. (2013), who inferred a minimum mass of $0.260 \pm 0.010 M_{\odot}$ from the host star’s RV trend.

Our mass of $M = 0.591 \pm 0.011 M_{\odot}$ is the first precise dynamical mass for the WD companion and agrees with the dynamical mass lower limit from Crepp et al. (2013). Comparing to the WD’s spectroscopic masses, it is the closest ($\approx 3\sigma$) to the mass of $0.54 \pm 0.01 M_{\odot}$ by Matthews et al. (2014), suggesting that the WD has a C/O core. Our orbital period of $108.2^{+5.2}_{-4.8}$ yr and inclination of $88.86^{\circ} \pm 0.21^{\circ}$ agree reasonably with $P \approx 124$ yr and $i = 88.11^{\circ} \pm 0.11^{\circ}$ published by Gratton et al. (2021). Our semimajor axis of $26.25^{+0.71}_{-0.66}$ au and eccentricity of 0.690 ± 0.017 are slightly smaller than $a = 30.11 \pm 0.03$ au and $e = 0.89$ by Gratton et al. (2021) because those authors assumed a companion mass higher than the dynamical mass we found. Other orbital parameters of the system are summarized in Table A4.

4.2.5 HD 118475

Because we fitted only to the RV data, there are no informative constraints on the orbital inclination. Instead of a precise dynamical mass, we obtain a minimum mass of $M_{\text{sec}} \sin i = 0.461^{+0.017}_{-0.015} M_{\odot}$, agreeing with $M_{\text{sec}} \sin i = 0.445 \pm 0.025$ from Kane et al. (2019), using the same RVs but a different fitting procedure. Other parameters ($a = 3.76^{+0.07}_{-0.06}$ au, $P = 2070.47 \pm 0.16$ d, $e = 0.128 \pm 0.001$, $\omega = 237.8^{\circ} \pm 0.2^{\circ}$) are nearly identical to the values in Kane et al. (2019) ($a = 3.69 \pm 0.11$ AU, $P = 2070.47^{+0.19}_{-0.2}$ d, $e = 0.128 \pm 0.001$, $\omega = 237.7^{\circ} \pm 0.3^{\circ}$). The complete set of orbital parameters is listed in Table A5.

In *Gaia* DR3, HD 118 475 has a two-body solution, given in terms of P , e , time of periastron T_0 , and the Thiele–Innes constants A , B , F , G in units of mas (multiplied by the semimajor axis of the photocentre motion a_0). We first convert the Thiele–Innes constants into physical orbit parameters with the following equations:

$$a_0 = \sqrt{p + \sqrt{p^2 - q^2}} \quad (1)$$

$$i = \cos^{-1} \frac{q}{a_0^2} \quad (2)$$

$$\omega = \frac{r + s}{2} \quad (3)$$

$$\Omega = \frac{r - s}{2}, \quad (4)$$

with p , q , r , s defined to be

$$p \equiv \frac{1}{2} (A^2 + B^2 + F^2 + G^2) \quad (5)$$

$$q \equiv AG - BF \quad (6)$$

$$r \equiv \tan^{-1} \left(\frac{F - B}{G + A} \right) \quad (7)$$

$$s \equiv \tan^{-1} \left(\frac{F + B}{G - A} \right). \quad (8)$$

Because the primary star is much brighter than the companion, the system’s photocentre almost coincides with the primary. Therefore, the semimajor axis of the photocentre motion is approximately that of the primary motion, which is related to the total semimajor axis a by

$$a = \frac{M_{\text{tot}}}{M_{\text{sec}}} a_0. \quad (9)$$

We also have Kepler’s third law:

$$P^2 = \frac{a^3}{M_{\text{tot}}}, \quad (10)$$

where P is in years, a is in au, and $M_{\text{tot}} = M_{\text{pri}} + M_{\text{sec}}$ is in solar masses.

Combining equations (9) and (10), we get

$$M_{\text{sec}}^3 - (M_{\text{pri}} + M_{\text{sec}})^2 \frac{a_0^3}{P^2} = 0 \quad (11)$$

from which we solve for the companion mass M_{sec} , given a primary mass of $M_{\text{pri}} = 1.16 \pm 0.06 M_{\odot}$ (Kervella et al. 2019).

The last two columns of Table A5 compare the orbital elements from our RV fit to those from the *Gaia* DR3 astrometric solution. Both solutions tightly constrain M_{sec} , a , P , e , and the argument of periastron ω , and they agree remarkably well. Once the *Gaia* IAD are published, a joint analysis of *Hipparcos* IAD, *Gaia* IAD, and RV will place tight constraints on all orbital parameters. Our analysis is an example of verifying a *Gaia* orbital solution against orbital parameters derived by other means. The same procedure could be applied to a large sample of binary systems with known orbits to validate the *Gaia* two-body solutions.

Our $M_{\text{sec}} \sin i$ of $0.461^{+0.017}_{-0.015} M_{\odot}$ and the *Gaia* DR3 inclination of $53^{\circ} 1^{+4^{\circ} 8}_{-5^{\circ} 5}$ give a dynamical mass of $0.580^{+0.052}_{-0.039} M_{\odot}$. The precise dynamical mass is much greater than the minimum mass of $\approx 0.445 M_{\odot}$ in Kane et al. (2019), implying that if the companion were an MS star, it would have a magnitude more inconsistent with the non-detection in the direct imaging observations by Kane et al. (2019) than previously derived. Using ORVARA, we confirm that the separation between the primary star and the companion was ≈ 0.09 arcsec at the observation epoch, so we refer to fig. 3 of Kane et al. (2019) as the non-detection significance curve. According to evolutionary tracks in MESA Isochrones and Stellar Tracks (MIST; Choi et al. 2016), a $0.58 M_{\odot}$ MS star would be only ≈ 3.87 mag fainter, near 880 nm, than the $1.16 M_{\odot}$ primary at the current age (~ 4.1 Gyr) and metallicity ($[\text{Fe}/\text{H}] = 0.10$) of the system (Valenti & Fischer 2005). Hence, we can rule out an MS companion at a significance level of more than 8σ . The dynamical mass also eliminates the possibility that the companion is a neutron star or a black hole. Therefore, we conclude that HD 118 475 B is a WD.

4.2.6 HD 136138

Stefanik et al. (2011) inferred a WD mass of $M_{\text{WD}} = 0.79 \pm 0.09 M_{\odot}$ from the *IUE* spectrum of the system (Landsman et al. 1996), using C/O-core cooling models in Wood (1995). The authors also obtained a dynamical mass of $0.59 \pm 0.12 M_{\odot}$ from a joint fit of *Hipparcos* IAD and RV. Analysing only the RVs, we get a minimum dynamical

mass of $M \sin i = 0.389_{-0.080}^{+0.081} M_{\odot}$, agreeing well with the dynamical mass and $i = 42.9^{\circ} \pm 6.7^{\circ}$ in Stefanik et al. (2011) ($M \sin i = 0.395_{-0.091}^{+0.099} M_{\odot}$) but only marginally with the spectroscopic mass. With a semimajor axis of only $a = 1.65_{-0.12}^{+0.10}$ au, it is possible that the progenitor of the WD once transferred some of its mass to the giant primary. We investigate this possibility in Section 6.1. Our period of 509.6 ± 1.2 d, eccentricity of $e = 0.336_{-0.014}^{+0.015}$, and RV semi-amplitude of $6.22_{-0.11}^{+0.14} \text{ km s}^{-1}$ all agree reasonably with $P = 506.45 \pm 0.18$ d, $e = 0.3353 \pm 0.0056$, and $K = 6.340 \pm 0.044 \text{ km s}^{-1}$ in Stefanik et al. (2011).

HD 136 138 also has a two-body solution in *Gaia* DR3. We derive the corresponding orbital elements with equations (1)–(11) and list the results in the last column of Table A6. The *Gaia* solution gives a semimajor axis and $M \sin i$ almost identical to our RV solution, but it has a slightly larger (1.7σ) eccentricity, shorter (by 1.7σ) period, and larger (by 3.2σ) argument of periastron, all in moderate tension with our values.

4.2.7 HD 169889

Our dynamical mass of $0.526_{-0.037}^{+0.039} M_{\odot}$ is the first precise mass of the WD, consistent with the dynamical mass lower limit of $0.369 \pm 0.010 M_{\odot}$ from Crepp et al. (2018). The eccentricity of $e = 0.896_{-0.088}^{+0.064}$ is the largest in our sample. A large eccentricity is not uncommon because the eccentricity distribution of wide MS binaries with separations smaller than 100 au is nearly uniform (Hwang, Ting & Zakamska 2022), and the isotropic and adiabatic mass-loss of a star during the AGB phase does not modify the eccentricity of its orbit (Dosopoulou & Kalogera 2016) unless it once tidally interacted with a close companion. We discuss the possibility of such close tidal interactions in Section 6.1. Our fit to relative separation has a χ^2 of 32 for only five observations, suggesting that the relative astrometry in Crepp et al. (2018) may have underestimated uncertainties. Inflating the uncertainties to get a reduced χ^2 of 1 does not affect the results significantly. The WD only has two broad-band photometry measurements in the H band and the L' band, which are insufficient to precisely measure its T_{eff} , $\log(g)$, or photometric mass (see Crepp et al. 2018, and our attempt in Section 6.2). Additional photometry or spectroscopy will be necessary to characterize the fundamental properties of the WD.

5 WD AGE INFERENCE

A dynamical mass comes directly from the solution to the Kepler problem, independent of stellar models and their theoretical uncertainties. Hence, it is a reliable starting point to constrain the fundamental parameters of a WD or test WD evolutionary models. A Sirius-like binary system is an especially ideal testing ground because the age of the system is often known by measuring the activity or the rotation of the MS star. The dynamical mass of the WD, closely related to the WD's cooling age and progenitor lifetime, allows for an independent measurement of the system's age. In this section, we outline our methods to infer the MS lifetimes and the cooling ages of the WDs and discuss our results for each system.

5.1 MS lifetime

The mass of a WD implies the mass of its MS progenitor, and the progenitor mass determines the progenitor's lifetime before evolving into a WD. We adopt the empirical IFMR in El-Badry, Rix & Weisz (2018) to compute the likelihood of a WD's progenitor mass from its

dynamical mass posterior in the MCMC chain. Then, we multiply the distribution with the initial mass function (IMF) in Chabrier (2003) (corrected for binaries) to obtain the posterior distribution of the initial mass. Finally, we perform cubic spline interpolation on MIST evolutionary tracks (Choi et al. 2016) to find the MS lifetime distribution from the initial mass posterior, assuming that the WD companion has the same metallicity as the MS primary. We remove any probability density beyond the age of the Universe (Planck Collaboration VI 2020, 13.8 Gyr) and re-normalize the distribution.

Our analysis is subject to potential systematics in our choice of IFMR, IMF, and stellar evolutionary model. We repeat the above procedures with the Cummings et al. (2018) IFMR, the Kroupa (2001) IMF, and evolutionary tracks from the PAdova and TRieste Stellar Evolution Code (PARSEC; Bressan et al. 2012), confirming that our conclusions in Section 5.3 do not change significantly.

5.2 Cooling age

The cooling age of a WD relates primarily to the starting condition of cooling (decided by its mass) and by how much it has cooled (its present effective temperature). A dynamical mass alone does not constrain the cooling age, but when paired with a T_{eff} measurement or multiband photometry, it tightens existing constraints. We perform multidimensional linear interpolation on the latest generation of Montréal cooling sequences² (Bédard et al. 2020) to compute the cooling age from dynamical mass and other parameters, assuming a pure-hydrogen (DA) atmosphere and a C/O core. The synthetic photometry in the Montréal cooling sequences is computed using prescriptions in Holberg & Bergeron (2006) and relies on models of Blouin, Dufour & Allard (2018), Tremblay et al. (2011), and Bédard et al. (2020) for low, intermediate, and high-temperature DA WDs, respectively. Our interpolation method is similar to that in Kiman et al. (2022).

5.3 Results

We place informative constraints on the ages of all WDs in this work except HD 27 786 Ab, HD 118 475 B, and HD 136 138 B. The unusually low mass of HD 27 786 Ab is smaller than the applicable range of the El-Badry et al. (2018) IFMR and the Cummings et al. (2018) IFMR and is not explainable by standard single-star evolutionary tracks. One needs to consider binary interaction to infer the age of the WD. HD 118 475 B and HD 136 138 B only have dynamical mass lower limits. The corresponding upper limits on age are over the age of the Universe. We present our results for the rest of the systems below.

5.3.1 HD 19019

The precision of our dynamical mass is insufficient to place good constraints on the MS lifetime of HD 19019 B. A considerable fraction of the mass posterior is below the applicable range of any IFMRs. If we naively apply the El-Badry et al. (2018) IFMR, we would obtain a progenitor mass of $M_{\text{pro}} = 2.8_{-1.3}^{+2.3} M_{\odot}$ and a maximum likelihood MS lifetime of ~ 0.5 Gyr (assuming $[\text{Fe}/\text{H}] = -0.15$ as in Arentsen et al. 2019), but we cannot rule out any lifetime within the age of the Universe. If we instead adopt the spectroscopic

²<http://www.astro.umontreal.ca/bergeron/CoolingModels>

mass of $1.12 \pm 0.15 M_{\odot}$ (Landstreet & Bagnulo 2020), we would get a progenitor mass of $M_{\text{pro}} = 6.3_{-1.7}^{+1.9} M_{\odot}$ and an MS lifetime of 110_{-60}^{+320} Myr.

Because the spectroscopic analysis in Landstreet & Bagnulo (2020) gives a relatively hot T_{eff} of 18200 ± 3000 K, but our dynamical analysis favours small masses, we get a young cooling age of 51_{-44}^{+157} Myr. If adopting $\log(g) = 8.85 \pm 0.15$ in Landstreet & Bagnulo (2020) instead of our dynamical mass, we obtain a much older cooling age of 530_{-220}^{+380} Myr. Given that the age of the MS primary is ~ 3.0 Gyr (Landstreet & Bagnulo 2020), if the WD had a mass of $\sim 0.54 M_{\odot}$, it would have a cooling age of ~ 0.1 Myr and an MS lifetime of ~ 2.9 Myr for a $\sim 1.4 M_{\odot}$ progenitor, giving a consistent total age. This mass is within the 1σ interval of our dynamical mass.

5.3.2 HD 27483

HD 27483 is a member of the Hyades cluster. For the cluster, different age determination methods give values in moderate tension.

Perryman et al. (1998) determine an age of 625 ± 50 Myr from non-rotating stellar models. Brandt & Huang (2015) infer an age of 750 ± 100 Myr from rotational stellar models from Ekström et al. (2012). Gossage et al. (2018) infer a somewhat younger age of ≈ 680 Myr from models with a different treatment of stellar rotation (Paxton et al. 2013). Martín et al. (2018) report a younger age of 650 ± 70 Myr by determining the lithium depletion boundary of two members. De Gennaro et al. (2009) obtained an age of 648 ± 45 Myr by fitting the WD portion of the colour–magnitude diagram to stellar evolution models. Here, we present an independent age estimate for the Hyades by inferring the age of HD 27483 B.

The $0.798_{-0.041}^{+0.10} M_{\odot}$ WD has a $3.59_{-0.78}^{+1.43} M_{\odot}$ progenitor, which lived a lifetime of 350_{-180}^{+570} Myr, assuming a metallicity of $[\text{Fe}/\text{H}] = 0.04$ (Bochanski et al. 2018). The imprecision originates mainly from the uncertainty in the empirical IFMR. We neglect uncertainties in the MS lifetime from, e.g. the effects of stellar rotation (Brandt & Huang 2015); these would be $\lesssim 20$ per cent of the age. Using a theoretical IFMR, like the MIST IFMR described in Choi et al. (2016), would reduce statistical uncertainties but overlook the systematics in theoretical modelling.

The photometry of a WD constrains its effective temperature, mass, and hence the cooling age. To find the magnitudes of HD 27483 B from the Δm measurements in Table 3, we need precise magnitudes of the host star in the two filters. We adopt $K_{\text{pri}} = 5.062 \pm 0.018$ from Cutri et al. (2003) as the K -band apparent magnitude of the primary. However, we are unaware of any measurement of the primary’s $F218W$ magnitude. Hence, we apply the SPECIES package (Stolker et al. 2020) to compute the magnitude from synthetic photometry. We modelled the spectrum of the primary with the BT-NextGen model (Allard, Homeier & Freytag 2012), adopting $T_{\text{eff}} = 6549 \pm 80$ K, $\log(g) = 4.04$ from Casagrande et al. (2011), and $R = 2.02_{-0.11}^{+0.10} R_{\odot}$ and $[\text{Fe}/\text{H}] = 0.04_{-0.13}^{+0.15}$ from Bochanski et al. (2018). Integrating the model spectrum with the $F218W$ filter, we obtain an $F218W$ absolute magnitude of $5.29_{-0.24}^{+0.26}$ for HD 27483 A. Finally, we add the host star magnitudes to the contrast values in Table 3 and get $M_K = 11.47 \pm 0.06$ and $M_{F218W} = 8.40 \pm 0.30$ for the WD companion.

Comparing the WD absolute magnitudes to the Montréal cooling sequences, we get a cooling age of 61_{-17}^{+21} Myr, an effective temperature of 21000 ± 3000 K, and a photometric mass of $0.669_{-0.066}^{+0.079} M_{\odot}$. Our T_{eff} agrees well with the spectroscopic T_{eff} of 20790 ± 187 K (Joyce et al. 2018) but has a much larger uncertainty. The photometric

mass is in mild tension with (1.4σ below) our dynamical mass. The observed magnitudes depend mainly on the WD’s T_{eff} and size, while the size depends on the WD’s mass via the MRR (e.g. Joyce et al. 2018; Romero et al. 2019; Chandra et al. 2020). The Montréal cooling sequences match the photometry of HD 27483 B at a radius larger than that expected for a $0.8 M_{\odot}$ WD, suggesting a lower mass. The lower mass would, in turn, imply a less massive progenitor and a longer MS lifetime (and older Hyades age). We note that with $T_{\text{eff}} \approx 21000$ K, the WD has its emission peak at about 1400 \AA , much bluer than both photometric bands. Additional photometry at shorter wavelengths and a more precise dynamical mass will hopefully resolve the discrepancy.

Combining all of our constraints, we perform a joint analysis of photometry and dynamical mass, treating the dynamical mass as a prior when fitting the cooling sequences to the photometry. We get a mass posterior of $0.763_{-0.026}^{+0.034} M_{\odot}$ and a cooling age of 45_{-9}^{+12} Myr. The cooling time is slightly smaller than that from photometry alone due to the mass tension.

Adding the cooling age from the joint analysis to the MS lifetime, we get a total age of 400_{-180}^{+570} Myr. The left-hand panel of Fig. 3 compares our age posterior (blue histogram) to the 1σ intervals of previous age estimates (light orange region for Brandt & Huang 2015 and light pink region for Martín et al. 2018). Our current analysis does not have the precision to resolve the age tension, mainly due to the uncertainties in the semi-empirical IFMR. Reducing the dynamical mass uncertainty would improve the cooling age but have negligible effects on the precision of the MS lifetime. On the contrary, if one could reduce the uncertainty of the IFMR by a factor of 4, they would constrain the total age to 10 per cent (≈ 70 Myr), comparable to the precision of other age estimates of Hyades.

5.3.3 HD 114174

The El-Badry et al. (2018) IFMR gives a progenitor mass of $1.90_{-0.27}^{+0.30} M_{\odot}$ for the $0.591 \pm 0.011 M_{\odot}$ WD. The Cummings et al. (2018) IFMR suggests a smaller progenitor of $1.28 \pm 0.47 M_{\odot}$. We adopt the former mass because El-Badry et al. (2018) has more low-mass ($< 0.6 M_{\odot}$) WDs in their calibration sample. Comparing the progenitor mass to MIST tracks, we get an MS lifetime of $1.46_{-0.48}^{+0.84}$ Gyr (for a metallicity of $[\text{Fe}/\text{H}] = 0.056$ as in Casali et al. 2020).

Previous works on the WD reported disagreeing effective temperatures leading to discrepant cooling ages. Our dynamical mass and $T_{\text{eff}} = 4260 \pm 360$ K from Matthews et al. (2014) combining spectroscopy and photometry suggests a cooling age of $t_{\text{cool}} = 8.3_{-2.1}^{+1.9}$ Gyr, but assuming $T_{\text{eff}} = 5890 \pm 270$ K from Gratton et al. (2021) using the SPHERE integral-field spectrograph instead gives $t_{\text{cool}} = 2.40_{-0.41}^{+0.52}$ Gyr. Other T_{eff} measurements are too imprecise to constrain the cooling age. Summing the MS lifetime and the cooling age, the former T_{eff} corresponds to a total age of $8.3_{-2.1}^{+1.9}$ Gyr, while the latter gives a much younger age of $3.93_{-0.74}^{+0.98}$ Gyr. The middle panel of Fig. 3 compares the total age posterior of the WD, for different T_{eff} , to the 1σ intervals of existing age measurements for the primary. The total age from our dynamical mass and the Gratton et al. (2021) T_{eff} agrees remarkably with the primary’s gyrochronological age by Crepp et al. (2013) but only marginally with the isochronal age from Tucci Maia et al. (2016). On the contrary, the much older age from the Matthews et al. (2014) T_{eff} is consistent with Tucci Maia et al. (2016) but in moderate tension with Crepp et al. (2013). Additional spectroscopy will be necessary to resolve the T_{eff} discrepancy and confirm the age of the WD.

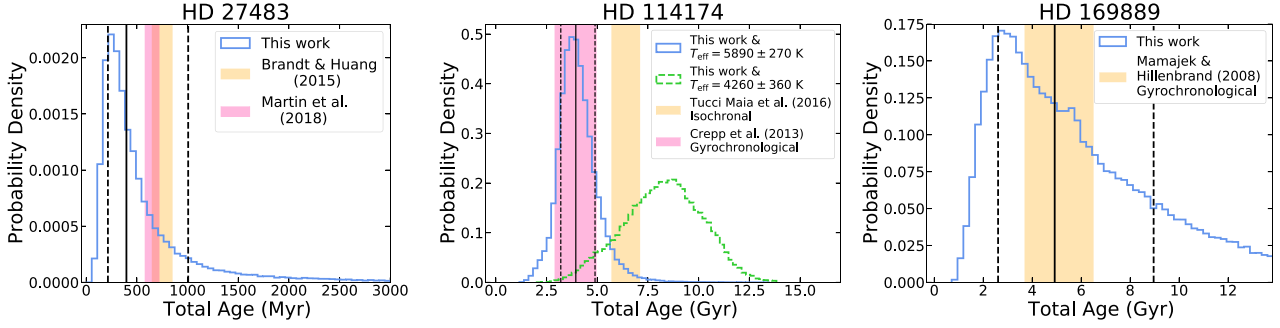


Figure 3. Comparison of the WD age posteriors (plotted as histograms) derived from our dynamical masses to the 1σ intervals (represented by shaded regions) of previous age measurements. In each panel, the vertical solid black line marks the 50th percentile of the distribution, while the two dashed black lines correspond to the 16th and the 84th percentiles. Left-hand panel (HD 27483): Our result does not resolve the age tension between Brandt & Huang (2015) (gold region, the age of the Hyades cluster derived from rotating isochrones) and Martin et al. (2018) (pink region, the lithium depletion boundary age of the Hyades cluster). Middle panel (HD 114174): Two discrepant T_{eff} give different ages. The age derived from $T_{\text{eff}} = 5890 \pm 270$ K (solid blue histogram, Gratton et al. 2021) agrees nicely with the primary’s gyrochronological age (pink region, Crepp et al. 2013), but the result from $T_{\text{eff}} = 4260 \pm 360$ K (dashed green histogram, Matthews et al. 2014) agrees better with the primary’s isochronal age (orange region, Tucci Maia et al. 2016). Right-hand panel (HD 169889): Our age constraint is loose but matches well with the primary’s gyrochronological age (orange region, Mamajek & Hillenbrand 2008).

5.3.4 HD 169889

The relatively light ($0.526^{+0.039}_{-0.037} M_{\odot}$) WD has a $1.33^{+0.38}_{-0.26} M_{\odot}$ progenitor, with an MS lifetime of $4.50^{+3.90}_{-2.38}$ Gyr (assuming $[\text{Fe}/\text{H}] = -0.14$ as in Brewer et al. 2016). Due to the uncertainty of the IFMR, our progenitor mass is not precise enough to rule out low-mass progenitors that lived up to the age of the Universe.

Crepp et al. (2018) could not determine the WD’s precise T_{eff} from their H -band and L' -band photometry, proposing two different temperatures consistent with observation. The cooler temperature, $T_{\text{eff}} \approx 2150$ K, plus our dynamical mass, would bring the cooling age to ≈ 12 Gyr, much longer than the primary’s gyrochronological age of $5.2^{+1.3}_{-1.5}$ Gyr (Mamajek & Hillenbrand 2008). The maximum likelihood total age would be even beyond the Universe’s age. A WD this cool and old has never been detected. Hence, we adopt the hotter temperature, $T_{\text{eff}} \approx 10\,000$ K, assuming a conservative uncertainty of 1000 K. We find a young cooling age of $0.48^{+0.20}_{-0.15}$ Gyr. The WD’s total age is, thus, $5.0^{+2.4}_{-2.4}$ Gyr, in good agreement with the primary’s gyrochronological age. The right-hand panel of Fig. 3 displays our age posterior on top of a shaded region representing the 1σ interval of the gyrochronological age. We cut the tail of the distribution at the Universe’s age. The age constraint could be considerably improved if one obtains a more precise IFMR in the low-mass range, ruling out light progenitors with extremely long lifetimes.

6 DISCUSSION

6.1 Orbital evolution and possible previous interactions in Sirius-like systems

A long-standing puzzle for many Sirius-like systems, including Sirius itself, is the lack of evidence of previous interactions despite the proximity of the binary during the WD progenitor’s AGB phase (see e.g. Oomen et al. 2018). For example, the progenitor of Sirius B was only ~ 1.5 – 1.6 au from Sirius A at the periastron, which is smaller than its radius in the AGB phase. However, the spectrum of Sirius shows no evidence of a common envelope event, nor did any component of Sirius deviate significantly from single-star evolutionary tracks (Bond et al. 2017). In addition, it is expected that when a star fills its Roche lobe substantially, its orbit tidally

circularizes on a time-scale shorter than that of stellar evolution (e.g. Bonačić Marinović, Glebbeek & Pols 2008), but Sirius B’s orbit remains eccentric ($e = 0.59$, Bond et al. 2017).

To investigate if our Sirius-like systems present similar puzzles, we derive the separations between the WD progenitors and their companions using their present-day orbital parameters. We assume that the mass-loss is adiabatic (on a time-scale much longer than the orbital period) so that (see derivations in, e.g. Dosopoulou & Kalogera 2016):

$$M_{\text{tot}} a = \text{constant} \quad (12)$$

$$e = \text{constant}. \quad (13)$$

Hence, we can compute the semimajor axis of the progenitor’s orbit, a_{pro} , from the current semimajor axis, the WD’s dynamical mass, the progenitor mass given by the IFMR, and the mass of the WD’s companion. Then, we take the progenitor’s orbital eccentricity to equal the present eccentricity, assuming that the orbit did not tidally circularize. Table 4 lists the eccentricity, the progenitor semimajor axis, the progenitor mass, and the mass ratio between the progenitor and its companion (now the primary star), $q_{\text{pro}} = M_{\text{pro}}/M_{\text{pri}}$, for five WDs. We take the present-day masses of HD 118475 B and HD 136138 B to be the masses from our $M_{\text{sin } i}$ and the *Gaia* DR3 inclinations. HD 19019 B and HD 27786 Ab are excluded because their dynamical masses are too small for existing IFMRs to give reliable progenitor masses.

The approximate radius of the Roche lobe of a star a separation A from its companion is given by (Eggleton 1983)

$$\frac{R_{\text{Roche}}}{A} = \frac{0.49q^{2/3}}{0.6q^{2/3} + \ln(1 + q^{1/3})}. \quad (14)$$

Here, we take A to be the separation between the WD progenitor and its companion at the periastron, $A = a_{\text{pro}}(1 - e)$. This gives the progenitor’s minimum Roche lobe radius along its orbit, $R_{\text{Roche, min}}$. We list the value of $R_{\text{Roche, min}}$ for each WD in the last column of Table 4.

HD 114174 B, HD 118475 B, HD 136138 B, and HD 169889 B have minimum Roche lobe radii comparable to or even smaller than the typical radius of a $\sim 2 M_{\odot}$ AGB star (~ 1 – 2 au), suggesting that they likely once filled their Roche lobes and transferred some

Table 4. Masses and orbital parameters of the progenitors.

HD	M_{pro} (M_{\odot})	q_{pro}	a_{pro} (au)	e	$R_{\text{Roche, min}}$ (au)
27483 B	$3.59^{+1.43}_{-0.78}$	$1.30^{+0.55}_{-0.31}$	$28.2^{+7.7}_{-5.5}$	$0.342^{+0.094}_{-0.19}$	$7.6^{+2.4}_{-1.6}$
114174 B	$1.90^{+0.30}_{-0.27}$	$1.96^{+0.32}_{-0.28}$	$14.3^{+1.5}_{-1.4}$	0.690 ± 0.017	2.18 ± 0.14
118475 B	$1.76^{+0.60}_{-0.43}$	$1.52^{+0.52}_{-0.38}$	2.24 ± 0.34	0.1278 ± 0.0008	$0.834^{+0.025}_{-0.029}$
136138 B	$1.69^{+0.87}_{-0.52}$	$0.94^{+0.55}_{-0.33}$	$1.11^{+0.20}_{-0.22}$	$0.336^{+0.015}_{-0.014}$	$0.235^{+0.032}_{-0.039}$
169889 B	$1.90^{+0.30}_{-0.27}$	$1.36^{+0.40}_{-0.28}$	$26.8^{+10.4}_{-7.3}$	$0.896^{+0.064}_{-0.088}$	$1.2^{+1.1}_{-0.7}$

of their masses to their companions. Yet, we are unaware of any observations of these systems that reported obvious signs of mass transfer. Moreover, the eccentricities of the systems are still high, contradicting the expectation that such close interactions would tidally circularize their orbits. These puzzles are very similar to those of Sirius, suggesting that the physics of interacting stars on the AGB phase is still poorly understood. Several mechanisms have been proposed to explain the high eccentricities of Sirius-like systems with close progenitors, such as eccentricity pumping due to phase-dependent mass-loss (Bonačić Marinović et al. 2008) and interactions with an unseen third component (Perets & Kratter 2012), but more work is needed to solve the puzzle for each system.

6.2 WD mass–radius relation

Theoretical models (e.g. Chandrasekhar 1931; Fontaine et al. 2001) predict an MRR of WDs at any given effective temperature. The MRR is crucial to our understanding of WDs and useful in inferring WD masses from photometry or spectroscopy when dynamical measurements are unavailable. In this section, we present additional data points to test the theoretical MRR by computing the radii of our WDs and comparing them to the dynamical masses we derived in Section 4.

We derive the radius of a WD by interpolating Montréal cooling sequences to compute the radius from multiband photometry. The interpolation method is similar to that used in finding the cooling ages. We successfully constrain the radii of HD 19019 B, HD 27483 B, HD 114174 B, and HD 169889 B with their available photometry. For HD 27786 Ab and HD 136138 B, we adopt the spectroscopic radius measurements in the literature, rescaled to their *Gaia* DR3 distances. Finally, as there are currently no photometric or spectroscopic observations of HD 118475 B, we postpone its radius measurement to future studies.

Table 5 lists the radii, dynamical masses, and effective temperatures of the WDs. We take the mass of HD 136138 B to be the mass from our $M \sin i$ and the *Gaia* DR3 inclination. Fig. 4 compares the positions of our WDs on the mass–radius diagram to the theoretical MRR given by Montréal cooling models at different effective temperatures. We note that this is equivalent to comparing a WD’s dynamical mass to its photometric mass, as theoretical models compute the photometric mass directly from the photometric radius and the MRR. Our WDs slightly deviate from but are statistically compatible with ($<2\sigma$ from) the theoretical MRRs at their effective temperatures. Below, we outline the photometry we adopted and elaborate on the results.

6.2.1 HD 19019 B

Because the WD was only resolved by *Gaia*, we adopt the *Gaia* DR3 photometry of $M_{\text{Gbp}} = 12.30 \pm 0.04$ and $M_{\text{Grp}} = 12.36 \pm 0.07$,

which give $T_{\text{eff}} = 14100 \pm 200$ K and $R = 0.887^{+0.023}_{-0.019} \times 10^{-2} R_{\odot}$. The results agree marginally with $T_{\text{eff}} = 18200 \pm 3000$ K and $R = 0.656^{+0.134}_{-0.112} \times 10^{-2} R_{\odot}$ from the spectroscopy in Landstreet & Bagnulo (2020). Because of the remarkable precision of *Gaia* photometry, our statistical uncertainties are likely smaller than the systematic uncertainties associated with our model assumptions (e.g. pure-hydrogen atmosphere). Therefore, the R and T_{eff} uncertainties listed in Table 5 should be considered lower bounds of the actual uncertainties, so it is unclear how much HD 19019 B agrees with the theoretical MRR.

6.2.2 HD 27483 B

From the K -band and the $F218W$ magnitudes in Section 5.3.2, we get $T_{\text{eff}} = 21000 \pm 3000$ K and $R = (1.252 \pm 0.095) \times 10^{-2} R_{\odot}$. The radius agrees remarkably with the spectroscopic radius of $R = (1.235 \pm 0.018) \times 10^{-2} R_{\odot}$ (Joyce et al. 2018). The photometry of the WD suggests a radius larger than that expected from the MRR, consistent with our finding in Section 5.3.2 that the WD’s photometric mass is 1.4σ below its dynamical mass.

6.2.3 HD 27786 Ab

Although we have measured the WD’s contrast with its host star in *HST* WFPC2 $F170W$ and WFC3 $F218W$ (Table 3), we are unaware of any measurements of the host star’s magnitudes in the two filters. We may estimate the host magnitudes from synthetic photometry, but the accuracy will be limited by the assumptions of our model spectrum. Also, both filters are very close to the peak of a blackbody emission (≈ 2000 Å for $T_{\text{eff}} \approx 14500$ as in Landsman et al. 1996), making it unlikely to constrain the WD’s T_{eff} and radius simultaneously. Hence, additional observations are required to reliably determine the WD’s photometric radius.

Landsman et al. (1996) fitted the WD’s radius and effective temperature from its *IUE* spectrum and obtained different values for a grid of different assumed distances. Interpolating the grid linearly to the *Gaia* DR3 distance of 42.03 ± 0.19 pc gives $T_{\text{eff}} = 14650 \pm 30$ K and $R = (1.741 \pm 0.015) \times 10^{-2} R_{\odot}$. The uncertainties reported here reflect only the parallax uncertainties and do not incorporate uncertainties in the original spectroscopic fitting, which are not provided in Landsman et al. (1996). Therefore, the actual error bars of R and T_{eff} are likely much larger. As shown in Fig. 4, the WD has a radius compatible with a C/O core despite its usually low mass.

6.2.4 HD 114174 B

We use $M_y = 14.09 \pm 0.05$, $M_J = 13.55 \pm 0.06$, $M_H = 13.44 \pm 0.03$, and $M_{K_s} = 13.11 \pm 0.02$, measured by Gratton et al. (2021) using SPHERE data, plus $M_{L'} = 13.18 \pm 0.16$ from Matthews et al. (2014)

Table 5. Radii, effective temperatures, and dynamical masses of the WDs.

HD	R ($0.01R_{\odot}$)	T_{eff} (K)	Reference	M (M_{\odot})
19019 B	$0.887^{+0.023}_{-0.019}$	14100 ± 200	This work	$0.32^{+0.37}_{-0.23}$
27483 B	1.252 ± 0.095	21000 ± 3000	This work	$0.798^{+0.10}_{-0.041}$
27786 Ab	$1.741 \pm 0.015^*$	$14650 \pm 30^*$	Landsman et al. (1996)	0.443 ± 0.012
114174 B	$1.15^{+0.15}_{-0.17}$	7200^{+1400}_{-1000}	This work	0.591 ± 0.011
136138 B	$1.314 \pm 0.011^*$	$29510 \pm 50^*$	Stefanik et al. (2011)	$0.531^{+0.092}_{-0.088}$
168889 B	$1.13^{+0.29}_{-0.23}$	10000 ± 1000	This work	$0.526^{+0.039}_{-0.037}$

Note. The R and T_{eff} of HD 27786 Ab and HD 136138 B are computed by interpolating the spectroscopic fit results in the listed references to the *Gaia* DR3 distances. The uncertainties here (marked with ‘*’) reflect only the parallax uncertainties and do not incorporate uncertainties of the spectroscopic fitting, which are likely much larger but are unavailable in the original references.

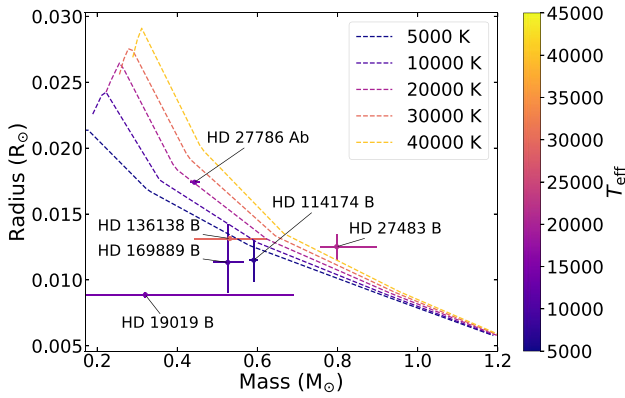


Figure 4. Masses and radii of six of our WDs (filled circles with 1σ error bars) compared to the theoretical MRRs given by Montréal cooling models (dashed lines). All data points and model curves are coloured according to their effective temperatures. Our WDs slightly deviate from but are statistically compatible with ($< 2\sigma$ from) the theoretical MRRs at their effective temperatures.

using NIRC2. When we fit Montréal cooling models to these measurements, the posterior distributions of T_{eff} and radius are bimodal, with one peak giving $T_{\text{eff}} = 5100$ K and $R = 1.71 \times 10^{-2} R_{\odot}$ and the other giving $T_{\text{eff}} = 9500$ K and $R = 0.75 \times 10^{-2} R_{\odot}$. This is likely related to the T_{eff} discrepancy discussed in Section 5.3.3. We attribute this to potentially underestimated systematic uncertainties from the calibration and data reduction of SPHERE observations, assuming that the statistical uncertainties reported by Gratton et al. (2021) are much smaller than the actual uncertainties. Given this assumption, we inflate the errors of all SPHERE photometry by 0.14 dex to achieve a reduced χ^2 of unity. Doing so leads to $T_{\text{eff}} = 7200^{+1400}_{-1000}$ K and $R = 1.15^{+0.15}_{-0.17}$, which are consistent with the WD’s dynamical mass within 1σ . Additional observations will be necessary to validate our assumption and resolve the discrepancy.

6.2.5 HD 136138 B

Due to the lack of photometry, we adopt the R and T_{eff} obtained by Stefanik et al. (2011) by fitting the WD’s *IUE* spectrum. Similar to our method for HD 27786 Ab, we interpolate the spectroscopic fit results to the *Gaia* DR3 distance of 110.97 ± 0.63 pc and get $T_{\text{eff}} = 29510 \pm 50$ and $R = (1.314 \pm 0.011) \times 10^{-2} R_{\odot}$. Again, these uncertainty values do not incorporate uncertainties of the

original spectroscopic fitting and should only be considered lower bounds of the actual uncertainties. At this radius and T_{eff} , the WD’s dynamical mass is slightly lower than the mass expected from the MRR.

6.2.6 HD 169889 B

$M_H = 13.59 \pm 0.16$ and $M_L = 13.32 \pm 0.08$ (Crepp et al. 2018) give $R = 1.13^{+0.29}_{-0.23} \times 10^{-2} R_{\odot}$ and a T_{eff} anywhere between ~ 4000 and ~ 12000 K. Our results are consistent with those in Crepp et al. (2018). As in Section 5.3.4, we assume $T_{\text{eff}} \approx 10000 \pm 1000$ K, noting that the uncertainty is a conservative estimate after ruling out cooler temperatures incompatible with the age of the host star. The uncertainties are large because both photometric measurements lie on the Rayleigh–Jeans tail of the WD’s spectrum, causing a degeneracy between T_{eff} and R . Assuming $T_{\text{eff}} = 10000$ K, additional photometry bluer than 14000 \AA will help break the degeneracy and determine how much the WD agrees with the theoretical MRR.

7 CONCLUSIONS

In this paper, we have derived the masses and orbits for six confirmed and one candidate Sirius-like systems from a joint analysis of high-precision RVs, relative astrometry, and *Hipparcos–Gaia* proper motion anomaly. From the dynamical masses of the WDs, we have constrained the ages of four systems and compared them to age estimates by other means. We have also discussed the possibilities of previous interactions between the WDs and their companions. Finally, we have derived the radii of the WDs and compared them to theoretical MRRs. We summarize our main results below:

(i) For HD 27483 B, our analysis of unpublished Hubble data and new observations with NIRC2 introduce two additional epochs of relative astrometry and photometry, allowing us to obtain the first-ever dynamical mass of the WD ($0.798^{+0.10}_{-0.041} M_{\odot}$). The ~ 10 percent-precision mass leads to a total age of 400^{+570}_{-180} Myr, consistent with previous age estimates of the Hyades cluster but not sufficiently precise to resolve the age discrepancy between various methods. Additional relative astrometry would improve the mass precision considerably, but the MS lifetime precision is limited by the calibration uncertainty of semi-empirical IFMRs. Constraints on the cooling age could be improved by additional photometry or adopting a T_{eff} from high-resolution spectroscopy.

(ii) Our three-body fit on HD 27 786 results in an unusually low mass ($0.443 \pm 0.012 M_{\odot}$) for the WD HD 27 786 Ab, suggesting the possibility of common envelope evolution with the primary star during its progenitor's AGB phase.

(iii) We obtain the first precise dynamical masses of HD 114 174 B ($0.591 \pm 0.011 M_{\odot}$) and HD 169 889 B ($0.526_{-0.037}^{+0.039} M_{\odot}$). The ages of both WDs depend strongly on the assumed T_{eff} , showing the need for high-resolution spectroscopy to resolve the T_{eff} uncertainty and improve the age constraints.

(iv) For HD 118475, the orbital elements we derived from RVs agree remarkably with the *Gaia* DR3 two-body solution from intermediate astrometry. Whereas for HD 136138, the best-fitting eccentricity and period from the RVs are in moderate tension with that from *Gaia*. Such a comparison, applicable to a large sample of systems, provides validations of *Gaia*'s two-body solutions.

(v) With $M \sin i = 0.461_{-0.015}^{+0.017} M_{\odot}$ and a *Gaia* DR3 inclination of $53^{\circ} 1_{-5^{\circ} 5}^{+4^{\circ} 8}$, HD 118 475 B has a dynamical mass of $0.580_{-0.039}^{+0.052} M_{\odot}$. By comparing the magnitude of a $0.58 M_{\odot}$ MS star to the non-detection significance curve in Kane et al. (2019), we rule out the hypothesis that the companion is an MS star at $>8\sigma$ level, confirming that it is a WD.

(vi) The progenitors of HD 114 174 B, HD 118 475 B, HD 136 138 B, and HD 169 889 B may have filled their Roche lobes during the AGB phase. Yet, their orbits did not tidally circularize, presenting a puzzle similar to that of Sirius.

(vii) The masses, radii, and effective temperatures of our WDs are compatible with the theoretical MRR from Montréal cooling models. In particular, HD 27 786 B has a radius consistent with a C/O core despite its usually low mass.

The precisions of such dynamical measurements of WD masses can reach ≈ 1 per cent for the very best stars. As shown in equation (8) of Brandt et al. (2019), this level of mass precision requires $\lesssim 1$ per cent precision each on separation, RV acceleration, and proper motion acceleration. Achieving this on all three measurements will be challenging for all but the best and closest targets, and the limiting factor will be different for each target. For example, HD 27 483 and HD 27 786 have multiple epochs of relative astrometry but no RVs. HD 118 475 and HD 136 138 have high-quality RV data over multiple orbital periods, but their orbital periods are too short for the *Gaia* proper motions to be helpful, nor do they have relative astrometry, preventing us from constraining their WD masses. The orbit fitting of HD 19 019 will benefit the most from proper motion measurements in a future *Gaia* release precise enough to detect its weak astrometric acceleration, while improving the orbit fitting of HD 169 889 requires better relative astrometry. Despite the challenges, continued RV and astrometric monitoring and exceptional data quality from future *Gaia* data releases will steadily grow the sample of WDs with very precise masses.

For WDs with better than ~ 15 per cent dynamical masses, such as HD 27 483 B, HD 114 174 B, and HD 169 889 B, the dominant source of age uncertainty (assuming a good T_{eff}) is the scatter in semi-empirical IFMRs. Theoretically modelled IFMRs, in comparison, are free from calibration uncertainties but replace them with systematic uncertainties of specific mass-loss models (e.g. Reimers 1975; Bloeker 1995). Hence, we choose not to use them to disentangle our analysis from systematics. From another perspective, our dynamical masses are themselves measurements of the IFMR. With a dynamical final mass, one can infer an initial mass, independent of mass-loss models, from the difference between the MS primary's age and the WD's cooling age. With help from precise astrometric solutions in *Gaia* DR3 and later releases, repeating our

analysis on additional Sirius-like systems would increase the sample size for a future recalibration of the WD IFMR.

ACKNOWLEDGEMENTS

We thank the anonymous referee for their thoughtful comments. This research has made use of the Set of Identifications, Measurements and Bibliography for Astronomical Data (SIMBAD, Wenger et al. 2000), operated at the Centre de Données astronomiques de Strasbourg (CDS), Strasbourg, France. This research has made use of the Spanish Virtual Observatory (SVO, <https://svo.cab.inta-csic.es>) Filter Profile Service (Rodrigo & Solano 2020) funded by MCIN/AEI/10.13039/501100011033/ through grant PID2020-112949GB-I00. This work has made use of data from the European Space Agency (ESA) mission *Gaia* (<https://www.cosmos.esa.int/gaia>), processed by the *Gaia* Data Processing and Analysis Consortium (DPAC, <https://www.cosmos.esa.int/web/gaia/dpac/consortium>). Funding for the DPAC has been provided by national institutions, in particular the institutions participating in the *Gaia* Multilateral Agreement. This research has made use of the Keck Observatory Archive (KOA), which is operated by the W. M. Keck Observatory and the NASA Exoplanet Science Institute (NExSci), under contract with the National Aeronautics and Space Administration (NASA). This research has made use of observations made with the NASA/ESA *Hubble Space Telescope*, and obtained from the Hubble Legacy Archive, which is a collaboration between the Space Telescope Science Institute (STScI/NASA), the Space Telescope European Coordinating Facility (ST-ECF/ESA), and the Canadian Astronomy Data Centre (CAD/C/NRC/CSA).

DATA AVAILABILITY

The observations used in this article are available in the Keck Observatory Archive (<https://koa.ipac.caltech.edu>), the Hubble Legacy Archive (<https://hla.stsci.edu>), and the references listed in Section 3.

REFERENCES

- Allard F., Homeier D., Freytag B., 2012, *Phil. Trans. R. Soc. A*, 370, 2765
 Althaus L. G., Serenelli A. M., Benvenuto O. G., 2001, *MNRAS*, 324, 617
 Arentsen A. et al., 2019, *A&A*, 627, A138
 Bacchus E. et al., 2017, *MNRAS*, 469, 4796
 Barstow M. A., Bond H. E., Burleigh M. R., Holberg J. B., 2001, *MNRAS*, 322, 891
 Bédard A., Bergeron P., Brassard P., Fontaine G., 2020, *ApJ*, 901, 93
 Bergeron P., Wesemael F., Beauchamp A., 1995, *PASP*, 107, 1047
 Beuzit J. L. et al., 2019, *A&A*, 631, A155
 Bloeker T., 1995, *A&A*, 297, 727
 Blouin S., Dufour P., Allard N. F., 2018, *ApJ*, 863, 184
 Bochanski J. J., Faherty J. K., Gagné J., Nelson O., Coker K., Smithka I., Desir D., Vasquez C., 2018, *AJ*, 155, 149
 Boehm-Vitense E., 1993, *AJ*, 106, 1113
 Boksenberg A., 1985, *Vistas Astron.*, 28, 531
 Bonačić Marinović A. A., Glebbeek E., Pols O. R., 2008, *A&A*, 480, 797
 Bond G., 1862, *Astron. Nachr.*, 57, 131
 Bond H. E. et al., 2015, *ApJ*, 813, 106
 Bond H. E. et al., 2017, *ApJ*, 840, 70
 Bowler B. P. et al., 2021, *AJ*, 161, 106
 Brandt T. D., 2018, *ApJS*, 239, 31
 Brandt T. D., 2021, *ApJS*, 254, 42
 Brandt T. D., Huang C. X., 2015, *ApJ*, 807, 58
 Brandt T. D., Dupuy T. J., Bowler B. P., 2019, *AJ*, 158, 140
 Brandt G. M., Argafal, trace andreason, 2021a, *gbrandt/HTOF*: 0.4.2

- Brandt T. D., Dupuy T. J., Li Y., Brandt G. M., Zeng Y., Michalik D., Bardalez Gagliuffi D. C., Raposo-Pulido V., 2021b, *AJ*, 162, 186
- Bressan A., Marigo P., Girardi L., Salasnich B., Dal Cero C., Rubele S., Nanni A., 2012, *MNRAS*, 427, 127
- Brewer J. M., Fischer D. A., Valenti J. A., Piskunov N., 2016, *ApJS*, 225, 32
- Brown J. M., Kilic M., Brown W. R., Kenyon S. J., 2011, *ApJ*, 730, 67
- Burleigh M. R., Barstow M. A., Holberg J. B., 1998, *MNRAS*, 300, 511
- Butler R. P. et al., 2017, *AJ*, 153, 208
- Cantat-Gaudin T., Brandt T. D., 2021, *A&A*, 649, A124
- Casagrande L., Schönrich R., Asplund M., Cassisi S., Ramírez I., Meléndez J., Bensby T., Feltzing S., 2011, *A&A*, 530, A138
- Casali G. et al., 2020, *A&A*, 639, A127
- Chabrier G., 2003, *PASP*, 115, 763
- Chandra V., Hwang H.-C., Zakamska N. L., Cheng S., 2020, *ApJ*, 899, 146
- Chandrasekhar S., 1931, *ApJ*, 74, 81
- Choi J., Dotter A., Conroy C., Cantiello M., Paxton B., Johnson B. D., 2016, *ApJ*, 823, 102
- Crepp J. R., Johnson J. A., Howard A. W., Marcy G. W., Gianninas A., Kilic M., Wright J. T., 2013, *ApJ*, 774, 1
- Crepp J. R. et al., 2018, *ApJ*, 864, 42
- Cummings J. D., Kalirai J. S., Tremblay P. E., Ramirez-Ruiz E., Choi J., 2018, *ApJ*, 866, 21
- Cutri R. M. et al., 2003, 2MASS All Sky Catalog of point sources, NASA/IPAC Infrared Science Archive, <http://irsa.ipac.caltech.edu/applications/Gator/>
- David T. J., Hillenbrand L. A., 2015, *ApJ*, 804, 146
- De Gennaro S., von Hippel T., Jefferys W. H., Stein N., van Dyk D., Jeffery E., 2009, *ApJ*, 696, 12
- Dembowski H., 1870, *Astron. Nachr.*, 76, 81
- de Medeiros J. R., Mayor M., 1999, *A&AS*, 139, 433
- Diego F., Charalambous A., Fish A. C., Walker D. D., 1990, in Crawford D. L., ed., *Proc. SPIE Conf. Ser. Vol. 1235, Instrumentation in Astronomy VII*. SPIE, Bellingham, p. 562
- Dosopoulou F., Kalogera V., 2016, *ApJ*, 825, 71
- Dufour P., Blouin S., Coutu S., Fortin-Archambault M., Thibeault C., Bergeron P., Fontaine G., 2017, in Tremblay P. E., Gaensicke B., Marsh T., eds, *ASP Conf. Ser. Vol. 509, 20th European White Dwarf Workshop*. Astron. Soc. Pac., San Francisco, p. 3
- ESA 1997, The HIPPARCOS and TYCHO Catalogues, ESA SP-1200
- Eggleton P. P., 1983, *ApJ*, 268, 368
- Ekström S. et al., 2012, *A&A*, 537, A146
- El-Badry K., Rix H.-W., Weisz D. R., 2018, *ApJ*, 860, L17
- Fischer D. A., Marcy G. W., Spronck J. F. P., 2014, *ApJS*, 210, 5
- Fontaine G., Brassard P., Bergeron P., 2001, *PASP*, 113, 409
- Foreman-Mackey D., Hogg D. W., Lang D., Goodman J., 2013, *PASP*, 125, 306
- Gaia Collaboration, 2016, *A&A*, 595, A1
- Gaia Collaboration, 2023, *A&A*, 674, A1
- Gomez Gonzalez C. A. et al., 2017, *AJ*, 154, 7
- Gossage S., Conroy C., Dotter A., Choi J., Rosenfield P., Cargile P., Dolphin A., 2018, *ApJ*, 863, 67
- Gratton R. et al., 2021, *A&A*, 646, A61
- Griffin R. F., 2009, *Observatory*, 129, 6
- Höfner S., Olofsson H., 2018, *A&AR*, 26, 1
- Holberg J. B., Bergeron P., 2006, *AJ*, 132, 1221
- Holberg J. B., Oswalt T. D., Sion E. M., Barstow M. A., Burleigh M. R., 2013, *MNRAS*, 435, 2077
- Holl B. et al., 2023, *A&A*, 674, A10
- Howard A. W. et al., 2010, *ApJ*, 721, 1467
- Hwang H.-C., Ting Y.-S., Zakamska N. L., 2022, *MNRAS*, 512, 3383
- Ivanova N. et al., 2013, *A&AR*, 21, 59
- Iwamoto K., Brachwitz F., Nomoto K., Kishimoto N., Umeda H., Hix W. R., Thielemann F.-K., 1999, *ApJS*, 125, 439
- Izmailov I. S., 2019, *Astron. Lett.*, 45, 30
- Jordan S., Napiwotzki R., Koester D., Rauch T., 1997, *A&A*, 318, 461
- Joyce S. R. G., Barstow M. A., Casewell S. L., Burleigh M. R., Holberg J. B., Bond H. E., 2018, *MNRAS*, 479, 1612
- Kallarakal V. V., Lindenblad I. W., Josties F. J., Riddle R. K., Miranian M., Mintz B. F., Klugh A. P., 1969, *Publ. U.S. Naval Obs. Second Ser.*, 18
- Kane S. R., Dalba P. A., Horner J., Li Z., Wittenmyer R. A., Horch E. P., Howell S. B., Everett M. E., 2019, *ApJ*, 875, 74
- Kervella P., Arenou F., Mignard F., Thévenin F., 2019, *A&A*, 623, A72
- Kilic M., Allende Prieto C., Brown W. R., Koester D., 2007, *ApJ*, 660, 1451
- Kiman R., Xu S., Faherty J. K., Gagné J., Angus R., Brandt T. D., Casewell S. L., Cruz K. L., 2022, *AJ*, 164, 62
- Knapp W., Nanson J., 2019, *J. Double Star Obs.*, 15, 42
- Konacki M., Lane B. F., 2004, *ApJ*, 610, 443
- Kroupa P., 2001, *MNRAS*, 322, 231
- Landsman W., Simon T., Bergeron P., 1996, *PASP*, 108, 250
- Landstreet J. D., Bagnulo S., 2020, *A&A*, 634, L10
- Latham D. W., 1992, in McAlister H. A., Hartkopf W. I., eds, *ASP Conf. Ser. Vol. 32, IAU Colloq. 135: Complementary Approaches to Double and Multiple Star Research*. Astron. Soc. Pac., San Francisco, p. 110
- Luhn J. K., Wright J. T., Howard A. W., Isaacson H., 2020, *AJ*, 159, 235
- Mamajek E. E., Hillenbrand L. A., 2008, *ApJ*, 687, 1264
- Marois C., Lafrenière D., Doyon R., Macintosh B., Nadeau D., 2006, *ApJ*, 641, 556
- Martín E. L., Lodieu N., Pavlenko Y., Béjar V. J. S., 2018, *ApJ*, 856, 40
- Mason B. D., Hartkopf W. I., Miles K. N., 2017, *AJ*, 154, 200
- Massarotti A., Latham D. W., Stefanik R. P., Fogel J., 2008, *AJ*, 135, 209
- Matthews C. T. et al., 2014, *ApJ*, 783, L25
- Mayor M., 1985, in Philip A. G. D., Latham D. W., eds, *Stellar Radial Velocities*. L. Davis Press, Schenectady, p. 21
- Morgan W. W., Harris D. L., Johnson H. L., 1953, *ApJ*, 118, 92
- Oomen G.-M., Van Winckel H., Pols O., Nelemans G., Escorza A., Manick R., Kamath D., Waelkens C., 2018, *A&A*, 620, A85
- Paxton B. et al., 2013, *ApJS*, 208, 4
- Perets H. B., Kratter K. M., 2012, *ApJ*, 760, 99
- Perlmutter S. et al., 1999, *ApJ*, 517, 565
- Perryman M. A. C. et al., 1998, *A&A*, 331, 81
- Phillips M. M., 1993, *ApJ*, 413, L105
- Planck Collaboration VI, 2020, *A&A*, 641, A6
- Rabe W., 1953, *Mikrometernmessungen von Doppelsternen in den Jahren 1932 bis 1946*
- Raghavan D. et al., 2010, *ApJS*, 190, 1
- Reimers D., 1975, *Mem. Soc. R. Sci. Liege*, 8, 369
- Riess A. G. et al., 1998, *AJ*, 116, 1009
- Rodrigo C., Solano E., 2020, *Contributions to the XIV.0 Scientific Meeting (virtual) of the Spanish Astronomical Society*. Spanish Astronomical Society, Barcelona, p. 182
- Romero A. D., Kepler S. O., Joyce S. R. G., Lauffer G. R., Córscico A. H., 2019, *MNRAS*, 484, 2711
- Rosenthal L. J. et al., 2021, *ApJS*, 255, 8
- Service M., Lu J. R., Campbell R., Sitarski B. N., Ghez A. M., Anderson J., 2016, *PASP*, 128, 095004
- Skiff B. A., 2014, *yCat*, 2023
- Skrutskie M. F. et al., 2010, in McLean I. S., Ramsay S. K., Takami H., eds, *Proc. SPIE Conf. Ser. Vol. 7735, Ground-Based and Airborne Instrumentation for Astronomy III*. SPIE, Bellingham, p. 77353H
- Stefanik R. P., Torres G., Latham D. W., Landsman W., Craig N., Murrett J., 2011, *AJ*, 141, 144
- Stolker T. et al., 2020, *A&A*, 635, A182
- Tokovinin A., Kiyava O., 2016, *MNRAS*, 456, 2070
- Tokovinin A., Mason B. D., Mendez R. A., Horch E. P., Briceño C., 2019, *AJ*, 158, 48
- Tremblay P. E., Bergeron P., Gianninas A., 2011, *ApJ*, 730, 128
- Tucci Maia M., Ramírez I., Meléndez J., Bedell M., Bean J. L., Asplund M., 2016, *A&A*, 590, A32
- Valenti J. A., Fischer D. A., 2005, *ApJS*, 159, 141
- Vogt S. S. et al., 1994, in Crawford D. L., Craine E. R., eds, *Proc. SPIE Conf. Ser. Vol. 2198, Instrumentation in Astronomy VIII*. SPIE, Bellingham, p. 362
- Vogt S. S. et al., 2014, *PASP*, 126, 359

- Vousden W. D., Farr W. M., Mandel I., 2016, *MNRAS*, 455, 1919
 Vousden W., Farr W. M., Mandel I., 2021, Astrophysics Source Code Library, record ascl:2101.006
 Wenger M. et al., 2000, *A&AS*, 143, 9
 Wertz O., Absil O., Gómez González C. A., Milli J., Girard J. H., Mawet D., Pueyo L., 2017, *A&A*, 598, A83
 Wizinowich P. et al., 2000, *PASP*, 112, 315
 Wood M. A., 1995, in Koester D., Werner K., eds, White Dwarfs, Vol. 443. p. 41
 Zeng Y. et al., 2022, *AJ*, 164, 188

SUPPORTING INFORMATION

Supplementary data are available at *MNRAS* online.

suppl_data

Please note: Oxford University Press is not responsible for the content or functionality of any supporting materials supplied by the authors. Any queries (other than missing material) should be directed to the corresponding author for the article.

APPENDIX A: FIGURES AND TABLES OF FIT RESULTS

Table A1. Posteriors of the HD 19019 system.

Parameter	Prior distribution	Posteriors $\pm 1\sigma$
Fitted parameters		
Primary mass (M_{\odot})	1.06 ± 0.06	$1.061^{+0.057}_{-0.062}$
Companion mass (M_{\odot})	Uniform	$0.32^{+0.37}_{-0.23}$
Parallax (mas)	31.979 ± 0.029	31.979 ± 0.028
Semimajor axis a (au)	$1/a$ (log-flat)	276^{+64}_{-47}
Inclination i ($^{\circ}$)	$\sin i$	$52.8^{+9.0}_{-15}$
$\sqrt{e} \sin \omega$	Uniform	$0.18^{+0.42}_{-0.43}$
$\sqrt{e} \cos \omega$	Uniform	$0.53^{+0.24}_{-0.26}$
Mean longitude at $t_{\text{ref}} = 2455197.50$ JD ($^{\circ}$)	Uniform	207^{+22}_{-11}
PA of the ascending node Ω ($^{\circ}$)	Uniform	23^{+326}_{-14}
RV jitter σ (m s^{-1})	Log-flat over $[0, 1000 \text{ m s}^{-1}]$	$12.2^{+2.6}_{-2.0}$
Derived parameters		
Orbital period (yr)	...	3888^{+1304}_{-956}
Semimajor axis (mas)	...	8830^{+2031}_{-1518}
Eccentricity e	...	$0.54^{+0.18}_{-0.27}$
Argument of periastron ω ($^{\circ}$)	...	59^{+281}_{-40}
Time of periastron T_0 (JD)	...	$3033863^{+373450}_{-164261}$
Mass ratio	...	$0.30^{+0.35}_{-0.22}$

Table A2. Posteriors of the HD 27483 system.

Parameter	Prior distribution	Posteriors $\pm 1\sigma$
Fitted parameters		
Primary mass (M_{\odot})	2.77 ± 0.26	$2.86^{+0.25}_{-0.22}$
Companion mass (M_{\odot})	$1/M$ (log-flat)	$0.798^{+0.10}_{-0.041}$
Parallax (mas)	21.094 ± 0.032	21.094 ± 0.025
Semimajor axis a (au)	$1/a$ (log-flat)	$49.8^{+12}_{-5.4}$
Inclination i ($^{\circ}$)	$\sin i$	30^{+13}_{-15}
$\sqrt{e} \sin \omega$	Uniform	$0.07^{+0.41}_{-0.49}$
$\sqrt{e} \cos \omega$	Uniform	$0.01^{+0.47}_{-0.47}$
Mean longitude at $t_{\text{ref}} = 2455197.50$ JD ($^{\circ}$)	Uniform	156^{+80}_{-126}
PA of the ascending node Ω ($^{\circ}$)	Uniform	174^{+121}_{-159}
Derived parameters		
Orbital period (yr)	...	184^{+65}_{-30}
Semimajor axis (mas)	...	1050^{+250}_{-115}
Eccentricity e	...	$0.342^{+0.094}_{-0.19}$
Argument of periastron ω ($^{\circ}$)	...	163^{+141}_{-111}
Time of periastron T_0 (JD)	...	2474412^{+4137}_{-2469}
Mass ratio	...	$0.284^{+0.033}_{-0.024}$

Table A3. Posteriors of the HD 27786 system.

Parameter	Prior distribution	Posteriors $\pm 1\sigma$	Posteriors $\pm 1\sigma$
	(Both companions)	(HD 27786 Ab)	(HD 27786 B)
Fitted parameters			
Primary mass (M_{\odot})	1.540 ± 0.077	$1.714^{+0.061}_{-0.060}$	
Companion mass (M_{\odot})	Uniform	0.443 ± 0.012	$1.36^{+0.51}_{-0.41}$
Parallax (mas)	23.79 ± 0.11		23.87 ± 0.11
Semimajor axis a (au)	$1/a$ (log-flat)	$12.04^{+0.13}_{-0.14}$	183 ± 16
Inclination i ($^{\circ}$)	$\sin i$	$172.8^{+3.2}_{-4.0}$	$158.8^{+10}_{-9.2}$
$\sqrt{e} \sin \omega$	Uniform	$0.574^{+0.053}_{-0.16}$	$0.07^{+0.21}_{-0.26}$
$\sqrt{e} \cos \omega$	Uniform	$0.15^{+0.31}_{-0.37}$	$0.09^{+0.16}_{-0.21}$
Mean longitude at $t_{\text{ref}} = 2455197.50$ JD ($^{\circ}$)	Uniform	48^{+294}_{-34}	211^{+72}_{-140}
PA of the ascending node Ω ($^{\circ}$)	Uniform	199^{+35}_{-33}	221^{+67}_{-140}
Derived parameters			
Orbital period (yr)	...	$28.42^{+0.31}_{-0.28}$	1436^{+203}_{-251}
Semimajor axis (mas)	...	$287.4^{+3.3}_{-3.4}$	4357^{+385}_{-367}
Eccentricity e	...	$0.4016^{+0.0083}_{-0.0084}$	$0.074^{+0.085}_{-0.052}$
Argument of periastron ω ($^{\circ}$)	...	77^{+34}_{-32}	124^{+176}_{-82}
Time of periastron T_0 (JD)	...	2456909^{+29}_{-28}	$2648314^{+202895}_{-89023}$
Mass ratio	...	$0.2585^{+0.0059}_{-0.0050}$	$0.80^{+0.31}_{-0.25}$

Table A4. Posteriors of the HD 114174 system.

Parameter	Prior distribution	Posteriors $\pm 1\sigma$
Fitted parameters		
Primary mass (M_{\odot})	0.968 ± 0.044	0.955 ± 0.043
Companion mass (M_{\odot})	$1/M$ (log-flat)	0.591 ± 0.011
Parallax (mas)	37.8677 ± 0.0243	37.867 ± 0.016
Semimajor axis a (au)	$1/a$ (log-flat)	$26.25^{+0.71}_{-0.66}$
Inclination i ($^{\circ}$)	$\sin i$	88.86 ± 0.21
$\sqrt{e} \sin \omega$	Uniform	$0.8088^{+0.0044}_{-0.0048}$
$\sqrt{e} \cos \omega$	Uniform	$0.190^{+0.027}_{-0.029}$
Mean longitude at $t_{\text{ref}} = 2455197.50$ JD ($^{\circ}$)	Uniform	21.1 ± 2.1
PA of the ascending node Ω ($^{\circ}$)	Uniform	$169.31^{+0.53}_{-0.52}$
RV jitter σ (m s^{-1})	Log-flat over $[0, 1000 \text{ m s}^{-1}]$	$3.55^{+0.39}_{-0.34}$
Derived parameters		
Orbital period (yr)	...	$108.2^{+5.2}_{-4.8}$
Semimajor axis (mas)	...	994^{+27}_{-25}
Eccentricity e	...	0.690 ± 0.017
Argument of periastron ω ($^{\circ}$)	...	$76.8^{+1.9}_{-1.7}$
Time of periastron T_0 (JD)	...	2481070^{+1682}_{-1524}
Mass ratio	...	$0.620^{+0.033}_{-0.030}$

Table A5. Posteriors of the HD 118475 system.

Parameter	Prior distribution	Posteriors $\pm 1\sigma$	<i>Gaia</i> solution $\pm 1\sigma$
Fitted parameters			
Primary mass (M_{\odot})	1.158 ± 0.058	$1.154^{+0.056}_{-0.055}$...
Companion mass (M_{\odot})	$1/M$ (log-flat)	...	$0.557^{+0.08}_{-0.072}$
Parallax (mas)	29.537 ± 0.017	29.537 ± 0.017	29.537 ± 0.017
Semimajor axis a (au)	$1/a$ (log-flat)	$3.758^{+0.070}_{-0.060}$	3.68 ± 0.18
Inclination i ($^{\circ}$)	$\sin i$...	$53.1^{+4.8}_{-5.5}$
$\sqrt{e} \sin \omega$	Uniform	$-0.3024^{+0.0007}_{-0.0006}$	$0.07^{+0.06}_{-0.26}$
$\sqrt{e} \cos \omega$	Uniform	$-0.1907^{+0.0017}_{-0.0016}$	$0.34^{+0.06}_{-0.65}$
Mean longitude at $t_{\text{ref}} = 2455197.50$ JD ($^{\circ}$)	Uniform	44.52 ± 0.05	...
PA of the ascending node Ω ($^{\circ}$)	Uniform	...	212^{+11}_{-191}
RV jitter σ (m s^{-1})	Log-flat over $[0, 10 \text{ m s}^{-1}]$	$0.02^{+1.77}_{-0.02}$...
Derived parameters			
Companion minimum mass $M_{\text{sec}} \sin i$ (M_{\odot})	...	$0.461^{+0.017}_{-0.015}$	$0.444^{+0.081}_{-0.076}$
Orbital period (d)	...	2070.47 ± 0.16	1968.6 ± 154.0
Semimajor axis (mas)	...	$111.0^{+2.1}_{-1.8}$	108.6 ± 5.3
Eccentricity e	...	0.1278 ± 0.0008	0.143 ± 0.036
RV semi-amplitude K (m s^{-1})	...	$5560.3^{+8.1}_{-8.4}$...
Argument of periastron ω ($^{\circ}$)	...	237.76 ± 0.22	$19.5^{+191.7}_{-9.7}$
Time of periastron T_0 (JD)	...	2455344^{+77}_{-66}	2456380 ± 160
Mass ratio	...	$0.419^{+0.066}_{-0.025}$	$0.481^{+0.070}_{-0.061}$

Table A6. Posteriors of the HD 136138 system.

Parameter	Prior distribution	Posteriors $\pm 1\sigma$	<i>Gaia</i> solution $\pm 1\sigma$
Fitted parameters			
Primary mass (M_{\odot})	1.84 ± 0.40	$1.80^{+0.37}_{-0.39}$...
Companion mass (M_{\odot})	$1/M$ (log-flat)	...	$0.543^{+0.078}_{-0.080}$
Parallax (mas)	9.011 ± 0.051	9.011 ± 0.051	9.011 ± 0.051
Semimajor axis a (au)	$1/a$ (log-flat)	$1.65^{+0.10}_{-0.12}$	$1.66^{+0.10}_{-0.12}$
Inclination i ($^{\circ}$)	$\sin i$...	$46.5^{+5.6}_{-6.6}$
$\sqrt{e} \sin \omega$	Uniform	$0.377^{+0.025}_{-0.029}$	$0.557^{+0.043}_{-0.044}$
$\sqrt{e} \cos \omega$	Uniform	$0.438^{+0.028}_{-0.024}$	$0.325^{+0.052}_{-0.057}$
Mean longitude at $t_{\text{ref}} = 2455197.50$ JD ($^{\circ}$)	Uniform	$341.0^{+2.4}_{-2.6}$...
PA of the ascending node Ω ($^{\circ}$)	Uniform	...	$52.4^{+5.1}_{-5.4}$
RV jitter σ (m s^{-1})	Log-flat over $[0, 1000 \text{ m s}^{-1}]$	$0.07^{+9.94}_{-0.07}$...
Derived parameters			
Companion minimum mass $M_{\text{sec}} \sin i$ (M_{\odot})	...	$0.385^{+0.046}_{-0.056}$	$0.389^{+0.081}_{-0.080}$
Orbital period (d)	...	509.6 ± 1.2	505.0 ± 2.5
Semimajor axis (mas)	...	$14.88^{+0.89}_{-1.11}$	$14.94^{+0.93}_{-1.06}$
Eccentricity e	...	$0.336^{+0.015}_{-0.014}$	0.419 ± 0.046
RV semi-amplitude K (m s^{-1})	...	6218^{+135}_{-113}	...
Argument of periastron ω ($^{\circ}$)	...	$40.5^{+3.4}_{-3.5}$	$59.6^{+5.5}_{-5.0}$
Time of periastron T_0 (JD)	...	2455451^{+184}_{-157}	2455281 ± 8
Mass ratio	...	$0.24^{+0.15}_{-0.04}$	$0.297^{+0.035}_{-0.028}$

Table A7. Posteriors of the HD 169889 system.

Parameter	Prior distribution	Posteriors $\pm 1\sigma$
Fitted parameters		
Primary mass (M_{\odot})	0.980 ± 0.049	$0.983^{+0.048}_{-0.049}$
Companion mass (M_{\odot})	$1/M$ (log-flat)	$0.526^{+0.039}_{-0.037}$
Parallax (mas)	28.2794 ± 0.0259	28.2795 ± 0.0079
Semimajor axis a (au)	$1/a$ (log-flat)	41^{+15}_{-10}
Inclination i ($^{\circ}$)	$\sin i$	$101.7^{+12}_{-8.8}$
$\sqrt{e} \sin \omega$	Uniform	$0.901^{+0.035}_{-0.050}$
$\sqrt{e} \cos \omega$	Uniform	$-0.21^{+0.25}_{-0.18}$
Mean longitude at $t_{\text{ref}} = 2455197.50$ JD ($^{\circ}$)	Uniform	52^{+19}_{-23}
PA of the ascending node Ω ($^{\circ}$)	Uniform	149^{+10}_{-20}
RV jitter σ (m s^{-1})	Log-flat over $[0, 1000 \text{ m s}^{-1}]$	$4.3^{+2.6}_{-1.5}$
Derived parameters		
Orbital period (yr)	...	212^{+126}_{-75}
Semimajor axis (mas)	...	1154^{+419}_{-294}
Eccentricity e	...	$0.896^{+0.064}_{-0.088}$
Argument of periastron ω ($^{\circ}$)	...	103^{+11}_{-16}
Time of periastron T_0 (JD)	...	2466913^{+1550}_{-819}
Mass ratio	...	$0.536^{+0.048}_{-0.047}$

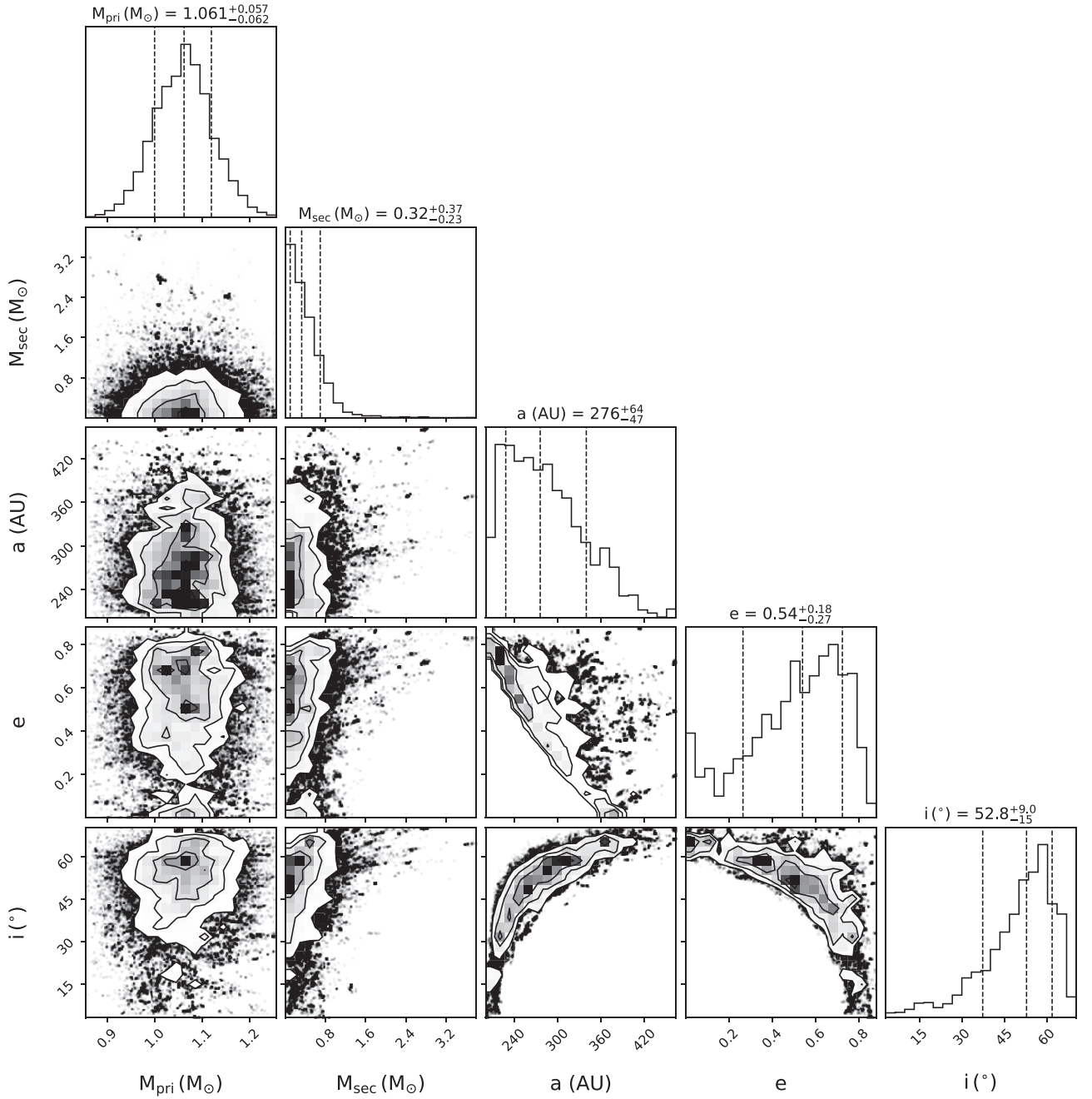


Figure A1. Best-fitting orbital parameters for the HD 19019 system and their posterior distributions from ORVARA. The selected parameters include the primary mass (in solar masses) M_{pri} , the secondary mass (in Jupiter masses) M_{sec} , the semimajor axis (in au) a , the eccentricity e , and the inclination (in degrees) i . The contours on the 2D joint posterior distributions give the 1σ , 2σ , and 3σ levels. The vertical dashed lines on the 1D marginalized distributions indicate the 16 per cent and 84 per cent quantiles.

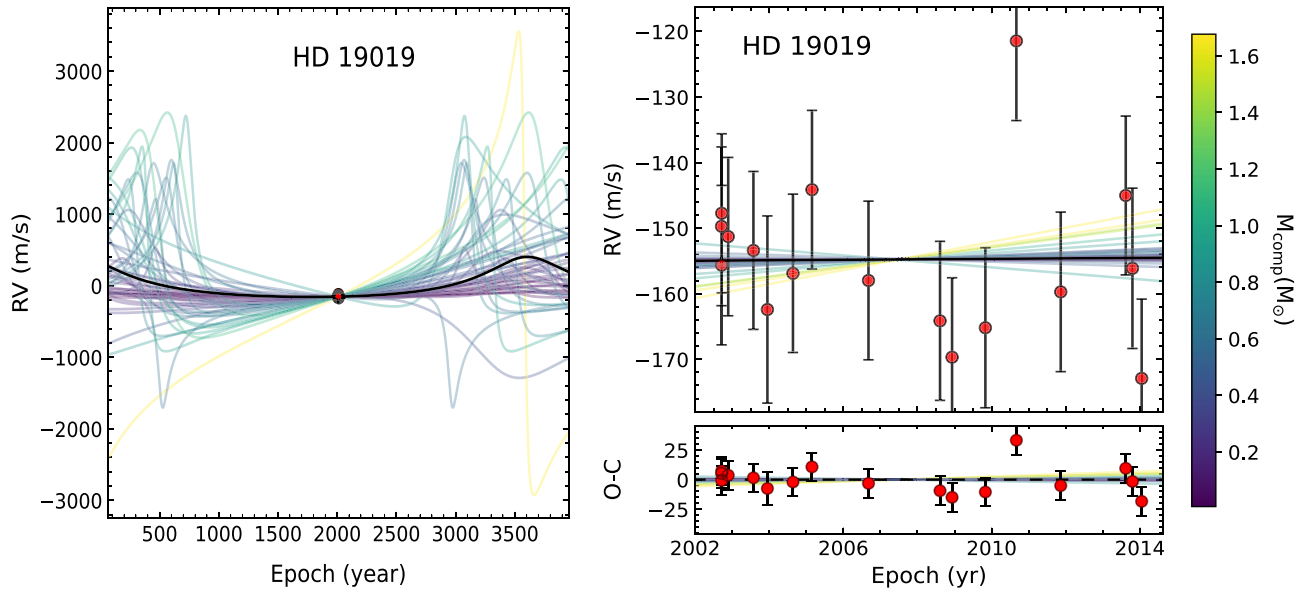


Figure A2. Left-hand panel: RV orbits of HD 19019 over the entire best-fitting orbital period. Right-hand panel: RV orbits of HD 19019 over the observational time frame (top) and the residuals after subtracting the best-fitting orbit (bottom). For both panels, an RV of zero corresponds to the barycentric velocity of the system. The thick black line indicates the maximum likelihood RV orbit. The thin lines, colour-coded by the companion mass, are 50 other orbits drawn randomly from the posterior distribution. The coloured dots are the RV measurements, with a different colour indicating a separate telescope. Most colour bars are too small to be visible in the left-hand panel.

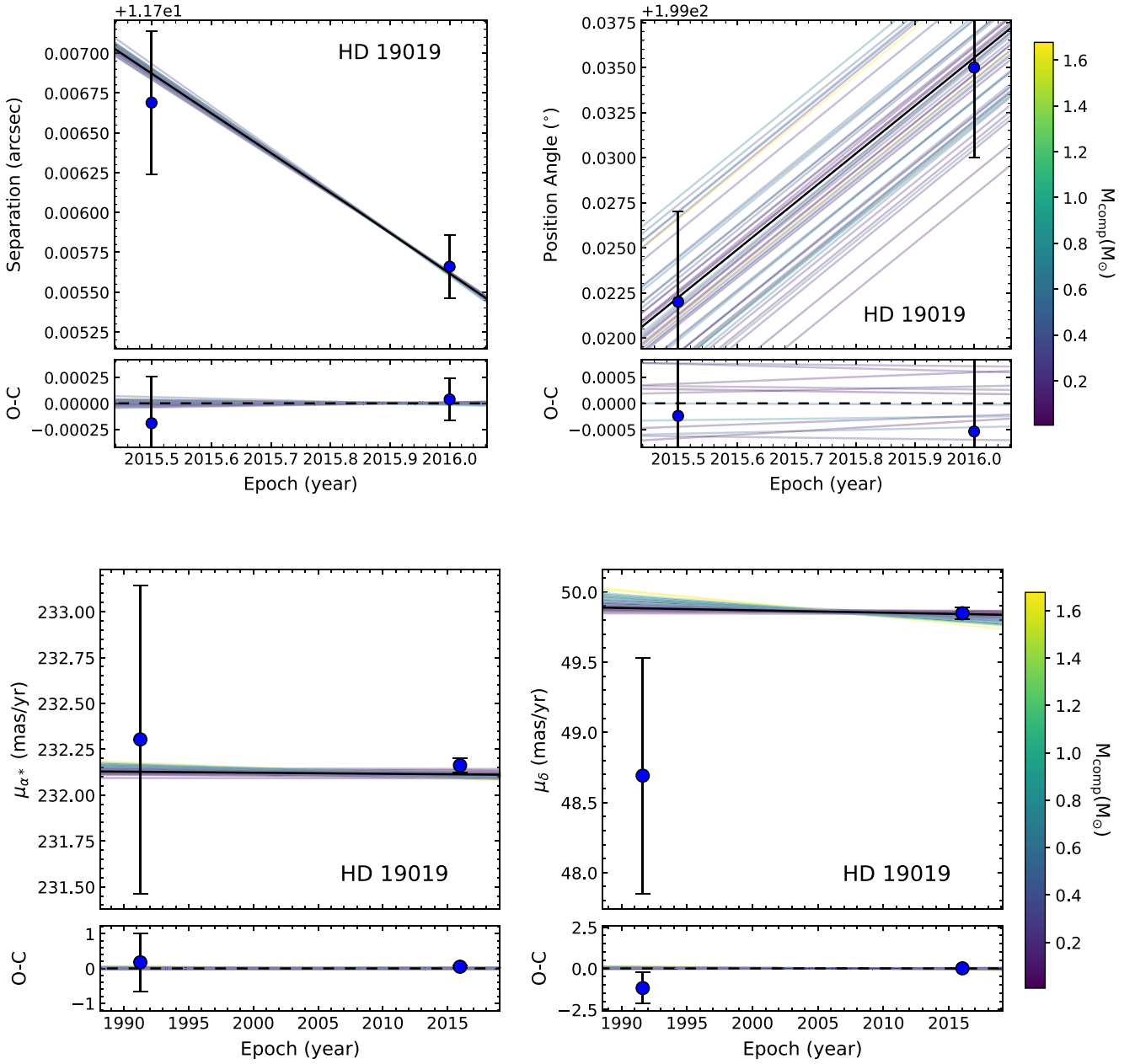


Figure A3. Relative (top panel) and absolute (bottom panel) astrometry for the HD 19019 system. The observations are shown as blue dots with error bars. The thick black line is the maximum likelihood orbit, and the thin lines, colour-coded by the companion mass, are 50 other orbits drawn randomly from the posterior distribution. The bottom part of each panel shows the residuals after subtracting the maximum likelihood orbit from the measurements.

This paper has been typeset from a $\text{\TeX}/\text{\LaTeX}$ file prepared by the author.